Dissertations and Theses   Dissertations and Theses

1979

A geophysical definition of a Klamath Falls graben fault

Cynthis Ann Veen
Portland State University

Recommended Citation

AN ABSTRACT OF THE THESIS OF Cynthia Ann Veen for the Masters of Science

in Geology presented September 14, 1979.

Title: A Geophysical Definition of a Klamath Falls Graben Fault.

APPROVED BY MEMBERS OF THE THESIS COMMITTEE:

Ansel G. Johnson, Chairman

Marvin H. Beeson

Gilbert T. Benson

        Four geophysical methods, along with well logs and outcrop data,

were used in determining the location of a fault situated on the campus

of Oregon Institute of Technology, just north of Klamath Falls, Oregon.

The fault displaces rocks of the Yonna Formation, of Pliocene age.

Wells located northeast of the fault (on the upthrown side) produce

cold water, and wells located southwest of the fault (on the down-

thrown side) produce hot water. The purpose of this investigation was

to define the characteristics of the fault exposed behind a large water

tank southeast of the OIT campus.

Approximately 100 gravity and magnetic stations were established along lines perpendicular to an assumed trend of the fault (N30W). Five resistivity lines, three northeast of the fault and two southwest of the fault were run. Three refraction profiles, one northeast of the fault, one southwest of the fault, and one across the fault, were run.

A cross section established from drillers' logs indicated the presence of two faults: the primary fault which is exposed near the campus, and a secondary fault located 45 to 75 m southwest of the primary fault. Both faults were included in gravity modelling, the primary process used in defining subsurface structure. Geologic control was provided by well logs and outcrop data. Resistivity data was used in establishing depths to some of the shallow interfaces. Refraction profiles were used to check gravity models.

Magnetic data indicated a significant low over the basalt just northeast of the fault. Although basalt normally has a higher magnetic susceptibility than tuff due to the presence of magnetite, oxidation of magnetite in basalt near the fault zone could cause the low observed in the data.

Gravity modelling of free air anomalies was done with a computer program obtained from the School of Oceanography, Oregon State University. Results of the modelling indicate that the two faults are parallel and trend approximately N35W. Dip on the primary fault is approximately 65 degrees SW, while the dip on the secondary fault may vary from 60 to 70 degrees SW. The southwest, or downdropped side of the fault is a tuff-filled basin which deepens to the north and west. The throw of the fault ranges from approximately 100 m in the south to 200 m in the

north, representing a slope of about 10 degrees. The primary fault
is probably located to within 15 m at the north end of the study
area, approximately 650 m northeast of its exposure.

A GEOPHYSICAL DEFINITION OF

A KLAMATH FALLS GRABEN FAULT

by

Cynthia Ann Veen

A thesis submitted in partial fulfillment of the
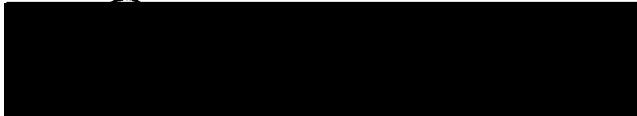requirements for the degree of

MASTER OF SCIENCE
in
GEOLOGY

Portland State University

1979

TO THE OFFICE OF GRADUATE STUDIES AND RESEARCH:

The members of the Committee approve the thesis of
Cynthia Ann Veen presented September 14, 1979.

Ansel G. Johnson, Chairman

Marvin H. Beeson

Gilbert T. Benson

APPROVED:

Ansel G. Johnson, Head, Department of Earth Sciences

Stanley E. Rauch, Dean of Graduate Studies and Research

ACKNOWLEDGMENTS

TABLE OF CONTENTS

LIST OF FIGURES

INTRODUCTION

The Klamath Falls area in southern Oregon exhibits geothermal phenomena (hot springs, hot water wells) related to structures of the Basin and Range province. With man's continuing social and technological development, recognition of the importance of alternative energy sources is increasing. Geothermal energy may reduce dependence on other resources of limited quantity, but it is a very localized resource and, has been detected only by physical manifestations such as hot springs and fumaroles.

Interest in developing exploration techniques for detection and delineation of geothermal areas is increasing. One method proposed for delineation of these resources is to monitor earth tidal strains (Bodvarsson, 1978). Earth tidal strains are dependent upon rock properties such as bulk modulus and rigidity. In areas where the bulk modulus and rigidity are reduced (such as near a magma chamber) straining of rocks should be easier, and earth tidal strains should be amplified. If a fault is present in the area, and the fault zone should be sufficiently less rigid than surrounding material, the fault should respond more easily to earth tides, and amplification should occur closest to the fault.

Since Klamath Falls exhibits geothermal phenomena related to fault structures, it provides an opportunity to test for earth tidal strain amplification. Under a grant from the U.S. Department of Energy, a series of strainmeters has been set up across a fault in the Klamath Falls area. However, to interpret the results of this monitoring, it

is important to know the location of the fault as precisely as possible. The purpose of this study was to use geophysical methods, along with well logs and outcrop data, to delineate the fault. Four types of geophysical surveys; gravity, magnetics, resistivity, and refraction, were conducted in the study area, and the combination of data from these surveys were used to construct several subsurface models which helped define the location of the fault.

LOCATION

Klamath Falls is located near the western edge of the Basin and Range province, in south-central Oregon, (Figure 1). The city lies at the southeastern tip of Upper Klamath Lake, at 42°12' latitude and 121°47' longitude, and has an elevation of approximately 1250 m above mean sea level. The Oregon-California border lies 25 kilometers to the south.

The study area includes a two square kilometer area on the eastern edge of the campus of Oregon Institute of Technology (OIT), approximately two kilometers north of Klamath Falls. The study area lies in Township 38 S, Range 9 E of the Willamette meridian and baseline, and includes parts of sections 16, 17, 20, and 21. The study area is located within the area checked on the map, west of Hogback Mountain. Campus Way, which turns east towards OIT off of Highway 97 just north of Klamaty Falls, provides road access to the area.

Oregon

SPRAGUE RIVER

UPPER

Modoc Pt.

KLAMATH

97

LAKE

140

SCALE
0 1 2 3 4 5 MILES
0 1 2 3 4 5 KILOMETERS
N

Whiteline Res.

Swan Lake

Hogback Mtn.
6198

KLAMATH FALLS

Round Lake

Altamont

140

140

39

Olene

LOST RIVER

66

KLAMATH RIVER

Lost River Diversion Canal

Kingsley Field

Nuss Lake

Keno

Midland

Stukel Mtn.
6525

Spring Lake

LOWER

KLAMATH HILLS

Hamaker Mtn.
6598

LOST

KLAMATH LAKEBED

Worden

39

97

Center Canal
Klamath Strait Drain

MERRILL

RIVER

42°30'

42°15'

42°00'

121°45'

Figure 1. Index map of Klamath Falls area. Thesis area is checked area west of Hogback Mtn. (Sammel and Peterson, 1976).

GEOLOGIC SETTING

Klamath Falls lies near the western edge of the Basin and Range province, where it meets with the Cascade Range. The area is characterized by large grabens flanked by northwest to north trending horsts. The faults dip at angles of greater than 60 degrees.

Rocks exposed in the area consist of sandstones, siltstones, ashy diatomites, basaltic tuffs and breccias, and basalt, grouped by Newcomb (1958) into the Yonna Formation, which is mid to late Pliocene in age. A generalized geologic map of the area is shown in Figure 2. Near Klamath Falls the Yonna Formation is covered only by a few late Tertiary and Quaternary basalt flows, evident as caprock on some of the higher ridges, and by Quaternary alluvium at the southeastern edge of Upper Klamath Lake and along the Klamath River. Older rocks do not crop out in the area, but have been interpreted from well logs to be lower Pliocene basalts (Peterson and McIntyre, 1970).

Two episodes of faulting are evident in the area. The first occurred prior to and during deposition of the Yonna Formation. These faults are characterized by consistency in trend (northwest to north) and closeness of spacing. Dips of exposed fault planes exceed 60 degrees. The faults exposed along the eastern side of Upper Klamath Lake belong to this group (Peterson and McIntyre, 1970).

North-south trending anticlines and synclines, formed after this first episode of faulting, appear to control the location of the second group of faults, lower Pleistocene in age. The density of these faults
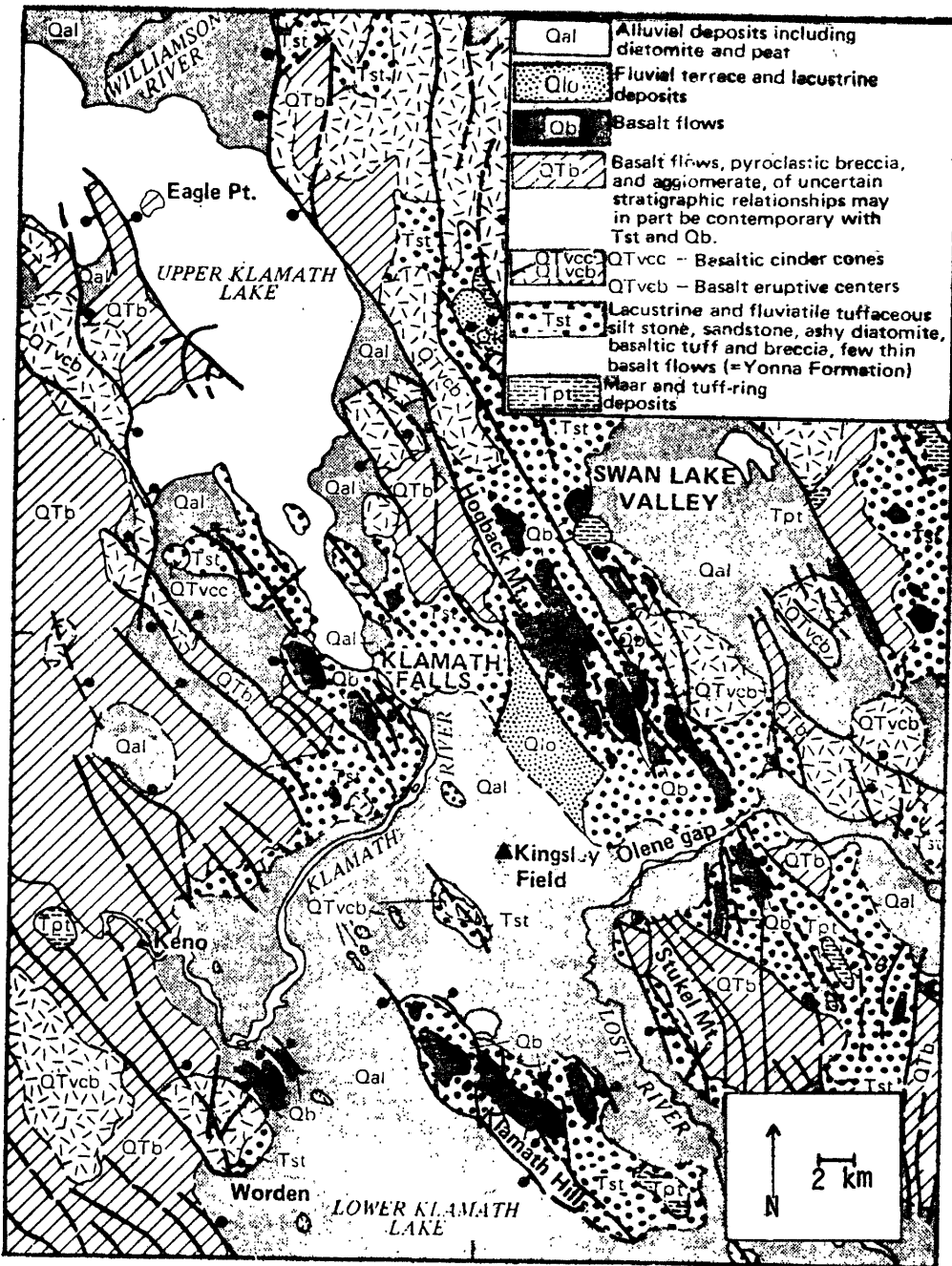
Figure 2. Geologic map of the Klamath Falls area (Sammel and Peterson, 1976).

increase in the vicinity of the anticlines and decrease in synclines (Peterson and McIntyre, 1970). This faulting is probably responsible for present day topography in the area, such as the large basin which contains Upper Klamath Lake. Movement of these faults is almost entirely in the dip slip direction, and displacement on some of the large faults has been estimated to be as much as 1800 m (6000 ft.) (Sammel and Peterson, 1976).

Tuff and basalt of the Yonna Formation are exposed in the thesis area. These outcrops, along with well logs from the three hot and three cold water wells drilled on the OIT campus provided geologic control for the gravity models. The well locations are shown in Figure 3, and a cross section containing four of the wells is shown in Figure 4. The units described as 'red lava' were used as marker beds in constructing the cross section. Well data shows interbedded tuffs and basalts of the Yonna Formation in the upper portion of the subsurface, with early Pliocene basalts below these. Logs from the cold wells located on the northeast, or upthrown side of the fault, contain more basalt in the upper portions than do well logs of the hot wells, located southwest of the fault. A photograph of the fault's exposure is shown in Figure 5, and its location is shown in Figure 3. A geologic map of the study area is shown in Figure 6.
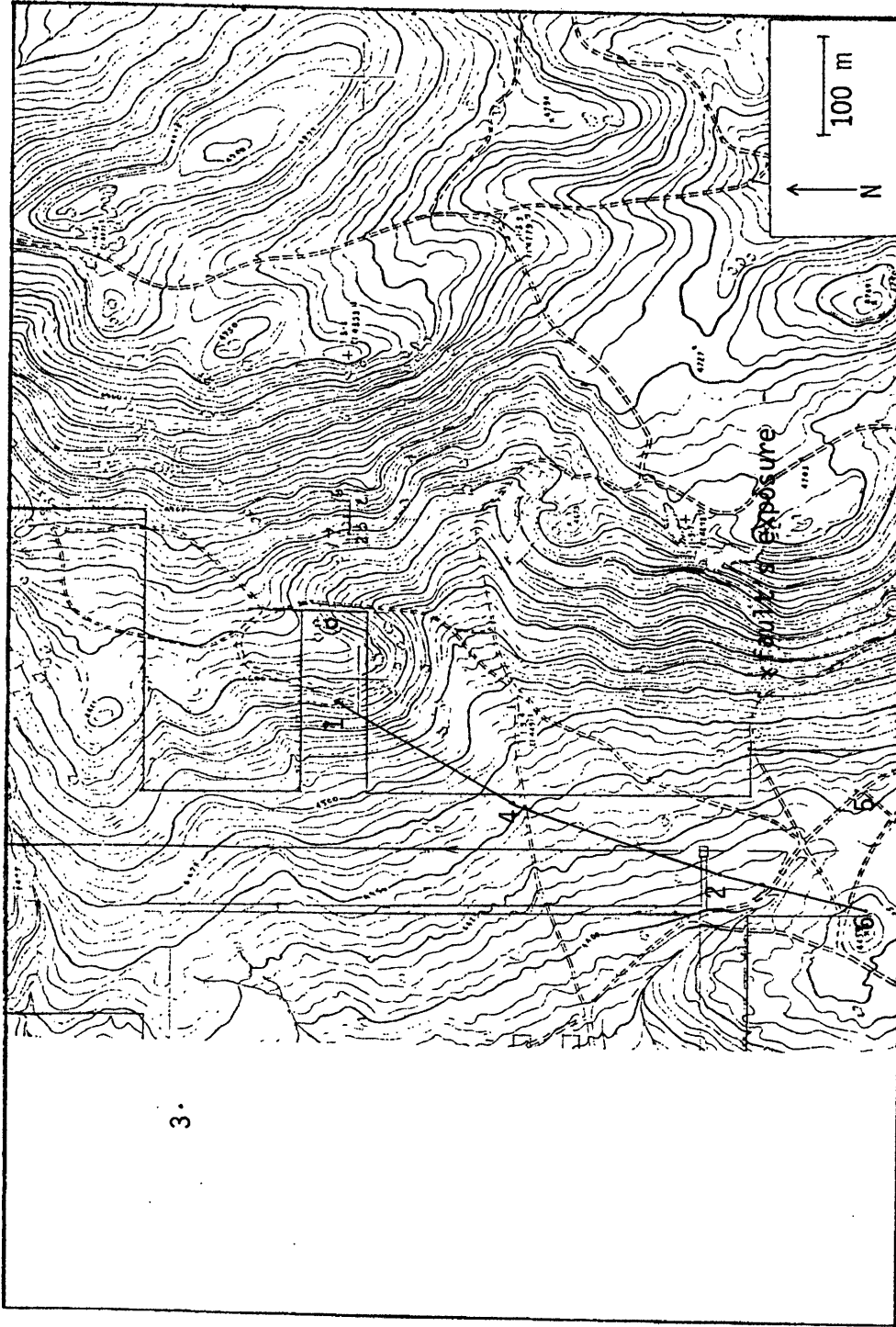
Figure 3. Water well locations on OIT campus. Wells 1, 3, and 4 are cold water wells; 2, 5, and 6 area hot water wells. Line of cross section is shown from wells 6, 2, 4, and 1.
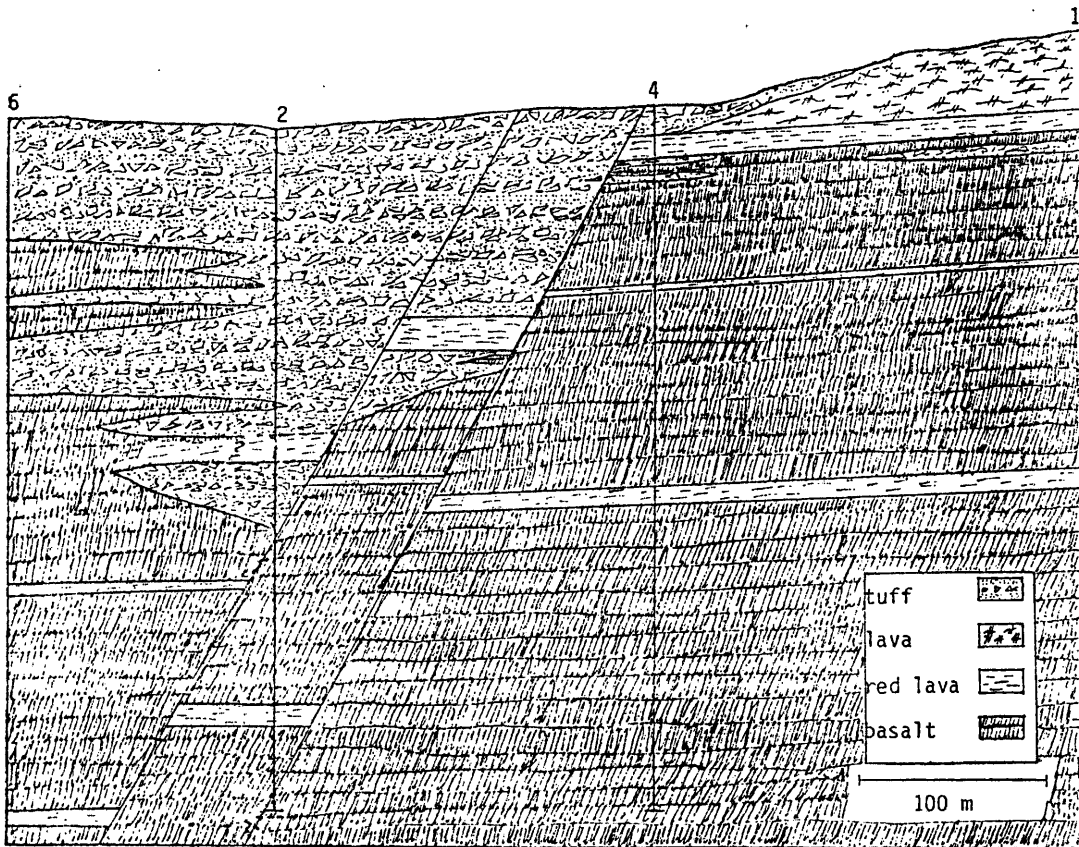
Figure 4. Geologic cross section using well log data from wells 6, 2, 4, and 1.

Figure 5. Photograph of fault's exposure on OIT campus.
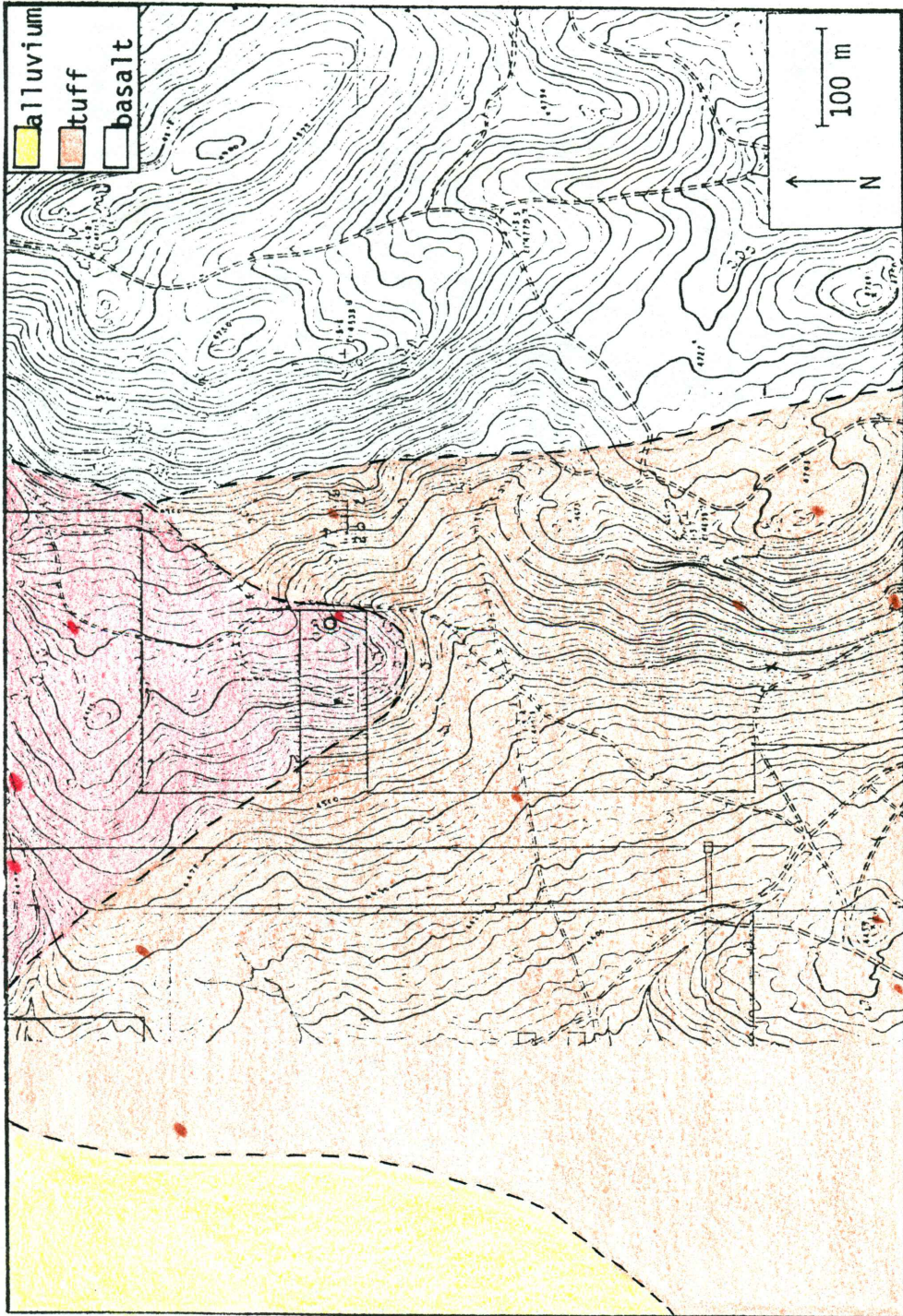
Figure 6. Geologic map of thesis area. Dark shaded areas are locations of outcrops.

GRAVITY

Gravity prospecting methods are based on the theory of attraction of two particles based on their masses and separation. Newton's law expresses this behavior in the equation: $F = \gamma m_1 m_2/r^2$, where m_1 and m_2 are the masses, r is the distance between the two centers of mass, and γ is the universal gravitational constant, 6.670×10^{-8} in the cgs system. The acceleration (g) of a body, m_2 due to the attraction of m_1 is obtained by dividing the force by m_2: $g = F/m_2 = \gamma m_1/r^2$. The units for g are cm/sec^2 and called the gal. The nominal value for g at the earth's surface is 980 gals. The rotation of the earth and its slightly oblate shape cause gravity values to be maximum at the poles and minimum at the equator, a difference of approximately 5.3 gals. This variation of gravity with latitude is expressed in the International Formula (1930): $g = 978.049(1 + 0.0052884 \sin^2\phi - 0.0000059 \sin^2 2\phi)$gals, where ϕ is the latitude (Dobrin, 1976).

Differences in values of g are also caused by lateral and vertical rock variations, and constitute the basis for gravity prospecting. These differences are extremely small in magnitude, and the milligal, or mgal (1/1000 gal) has been adopted to measure these changes. Modern gravimeters are capable of measuring changes in the earth's gravity field to several thousandths of a milligal, although routine work is measured to .01 mgal. In measuring gravity at points along the earth's surface, comparisons are made to the theoretical gravity (International Formula), the gravity that would exist at sea level at those points.

To compensate for elevation departures from sea level, several correc-
tions are made to the measurements: free air, Bouguer, and terrain
corrections.

Gravity theory states that the attraction between two particles
is measured as if the masses of the particles were concentrated at
their centers. The free air correction compensates for the fact that
stations above and below sea level will have different distances to the
center of the earth than if gravity was measured at sea level. At sta-
tions above sea level the attraction of masses is less, so the correc-
tion must be added. At stations below sea level, the correction is
subtracted. The value for the correction is .3086 mgal/m (.09406
mgal/ft.).

Correction must also be made for the fact that at stations above
sea level the attraction of the slab of material above sea level is
included in the gravity measurement. The gravity contributed by this
attraction must be subtracted from the measured gravity. At stations
below sea level, the attraction of a slab of material extending from
the elevation of that point to sea level is missing. A correction is
added to the measurement compensate. This correction is the Bouguer
correction, and its value is $2\pi\gamma\rho t$, where ρ is a standard reduction
density of 2.67 g/cc and t is the thickness of the slab.

The terrain correction compensates for effects of local topography
on gravity measurements. A mass is attracted to the earth not only by
material directly beneath it, but by material around it. Any local
topography changes the gravitational attraction at a point. The mass of
a nearby hill is an attractive force, and detracts from the gravity

that would be measured on a slab of uniform elevation. A valley is a mass deficit, and its effect is to also subtract from the gravity of a slab of uniform elevation. For elevations above and below the station, terrain corrections are added. An overlay of rings divided into compartments is used over topographic maps of the area to calculate the correction. The average elevation in each compartment is estimated, and the difference between that elevation and the elevation of the station is used in calculating a correction for that compartment. Corrections for all compartments are added to calculate the total terrain correction for that station.

When only the free air correction is made to the gravity measurements, the difference between the measured and the theoretical gravity at that point is called the free air anomaly. When free air and Bouguer corrections are made, that difference is called the simple Bouguer anomaly, and when the terrain correction is also added, the difference between the corrected measured gravity and the theoretical gravity is the complete Bouguer anomaly.

Field Work.

The gravity survey was conducted during February and March of 1979. Stations were first surveyed with a transit, using two benchmarks established by OIT and one section marker. Gravity readings were taken with a Worden gravimeter on loan from the School of Oceanography, Oregon State University. The base station used in the survey was part of the gravity base station network in Oregon tied directly with the international gravity base station at Carnegie Institution, Washington,

D.C. The base station is located at the base of the column at the southwest corner of the classroom building on the OIT campus, at the center of the radius of curvature of the depression in the column.

At some stations levelling the gravimeter was difficult due to muddy ground surface, but where possible, readings were repeated with an accuracy of approximately .03 mgal. Some of the readings could be reapeated to only .06 mgal. The base station was occupied at the beginning and end of each day and at approximately two hour intervals throughout the day. Temperature variations of the instrument were noted at each reading and later corrected for.

Data Reduction.

Data reduction consisted of drift, tidal, and terrain corrections done by hand; free air and Bouguer corrections were calculated with a computer program. Correction for instrument drift consisted of establishing a drift curve from base station readings. Readings from gravity stations were plotted on the curve and then corrected to the base level of the curve.

Tidal corrections were made using a computer program obtained from the School of Oceanography, Oregon State University. The program gives the tidal correction in mgals at one-half hour intervals, and corrections for readings taken at intermediate times were made by extrapolation.

Terrain corrections were made using the technique described in Dobrin (1976). Hammer charts consist of successive rings of compartments at greater radii from the station. Each ring is called a zone.

U.S. Geological Survey topographic maps were used in determining cor-
rections for zones E (radii of 558-1280 ft.) through M (radii of 48,365-
71,996 ft.). A topographic map of the OIT campus with a five foot con-
tour interval was used, along with field notes on topography, to deter-
mine corrections for zones B (radii of 6.56-54.6 ft.) through D (radii
of 175-558 ft.). Some of the stations did not fall within the bound-
aries of the campus map, and corrections for the inner zones of these
station were based upon field notes. For zone M, one terrain correction
was made and this value used for all stations. Values were computed
for every fourth station in zones E through L, with intermediate values
extrapolated, while corrections were made for each station in zones B
through D.

Free air and Bouguer corrections were done with a computed pro-
gram developed for this purpose. The program, GRAVPLOT (obtained from
the Earth Science Department, Portland State University), uses the In-
ternational Formula to determine free air and simple Bouguer anomalies.
The terrain corrections are programmed into the computer, and the com-
plete Bouguer anomaly is also computed. The free air, simple Bouguer,
and complete Bouguer anomalies are plotted against elevation by the
program. The reduced gravity data is listed in Appendix 1.

Errors for the gravity measurements were estimated to be:

  .03 mgals-gravity reading
  .03 mgals-drift
  .03 mgals-elevation
  .05 mgals-terrain correction
  .01 mgals-latitude

Since the errors are random, the total error is not the sum of the indi-
vidual errors, but might be better estimated by $\sqrt{\Sigma e^2}$ (A.G. Johnson,

personal communication). This method gives a combined error of .07 mgals.

Interpretation.

Six gravity lines, labeled A-F in Figure 7, were run in a direction perpendicular to the assumed trend of the fault (N30W). It was felt that this orientation would simplify not only gravity modelling of the area, but also the interpretation of the models. Station were spaced approximately 30 m apart near the fault, and up to 100 m apart away from the fault. Station locations are shown in Figure 7.

Geologic constraint for the models was provided by scattered basalt and tuff outcrops throughout the area, some resistivity data, and by well logs of six water wells located on the OIT campus, shown in Figure 3. The three hot wells are located on the southwest or downthrown side of the fault, and the three cold wells lie on the northeast or upthrown side of the fault. A cross section from well logs of four of the wells located on a nearly linear trend provided control for gravity line C. The gravity modelling was constrained by the two faults necessary in the cross section to be consistent with the well data (see Figure 4). Regional gravity control was obtained from free air and Bouguer anomaly maps of the Klamath Falls area (Van Deusen, 1977).

Gravity modelling was done with a computer program, FREEAIRFIT, developed for this purpose and described by Jones (1976). The program computes relative anomalies due to inhomogeneities in the subsurface. The gravitational effects of bodies of rock in two dimensions are computed; the third dimension is not considered. Areas of different

densities within the model are approximated by polygons, and the verti-
cal attraction of these polygons computed for each station. Corners of
the polygons are specified by X (horizontal) and Z (vertical) coordi-
nates; station locations for computing gravity are located in the same
manner.

No regional gradient was observed on regional free air anomaly
maps, and so was not included in the modelling. A regional free air
model was constructed to consider effects of the surrounding area on the
gravity profiles of the study area.

Three densities for rocks of the area were used in the modelling.
A density of 2.8 g/cc was used for basalt. This value is lower than
an average basalt density of 3.0 g/cc (Telford and others, 1976; Sharma,
1976) because basalt in the area is fractured (Sammel and Peterson,
1976). A value of 2.4 g/cc was used as the density of the tuffaceous
rocks. Rough density measurements were done on six samples of tuff from
the area, giving an average density of approximately 2.4 g/cc. A den-
sity contrast of .4 g/cc for these rocks is consistent with the density
contrast used by Peterson (Sammel and Peterson, 1976) to model an area
25 kilometers to the south. A surface density of 2.0 g/cc was used on
the southwest end of lines A and B. This area has been reworked due
to the presence of OIT buildings, and is also covered with alluvium
(see Figure 2). For these reasons, a 2.0 g/cc density assumption seems
reasonable. In the modelling program, it is the density contrast and
not the absolute density which is used to calculate anomalies. Eleva-
tion accuracy is important because the effect of a density contrast of
2.4 g/cc (air and tuff) is much more significant than a contrast of

4 g/cc (tuff and basalt).

Each gravity line was first considered separately and modelled
to be consistent with geologic information available for that line. A
gravity profile for a homogeneous body of rock was modelled for each
line to estimate gravity effects due to elevation changes only. Models
were constructed to a depth of 800 m above sea level; the anomaly below
this point is probably not apparent because the rock at depth on each
side of the fault is similar. When the model for each line was consis-
tent with available information and 'fit' the gravity profile for that
line relatively well, the models were refined to make them consistent
with each other. Line D, the southernmost line was discarded from the
modelling process. A regional gravity study of the area (Sammel and
Peterson, 1976) indicates a gravity high over the city of Klamath Falls,
shown in Figure 8. It was felt that the source of this high might be
affecting the gravity profile of line D, and the line was discarded
because is would not be useful in determining the location of the fault.
Two other short gravity lines, E and F were also completed. These lines
were not long enough to be modelled, but were used in constructing the
gravity anomaly contour map, shown in Figure 7. A total of approxi-
mately sixty models were attempted for gravity lines A, B, and C.

Line C. The southwest end of Line C, shown in Figure 7, is loca-
ted near the Presbyterian Intercommunity Hospital, and trends N60E.
The free air anomaly and associated model are shown in Figure 9. The
line crosses the geologic cross section (see Figure 4), between wells
number 6 and 2. Although geologic control for the cross section is
somewhat limited in this area, it was used in approximating depths and
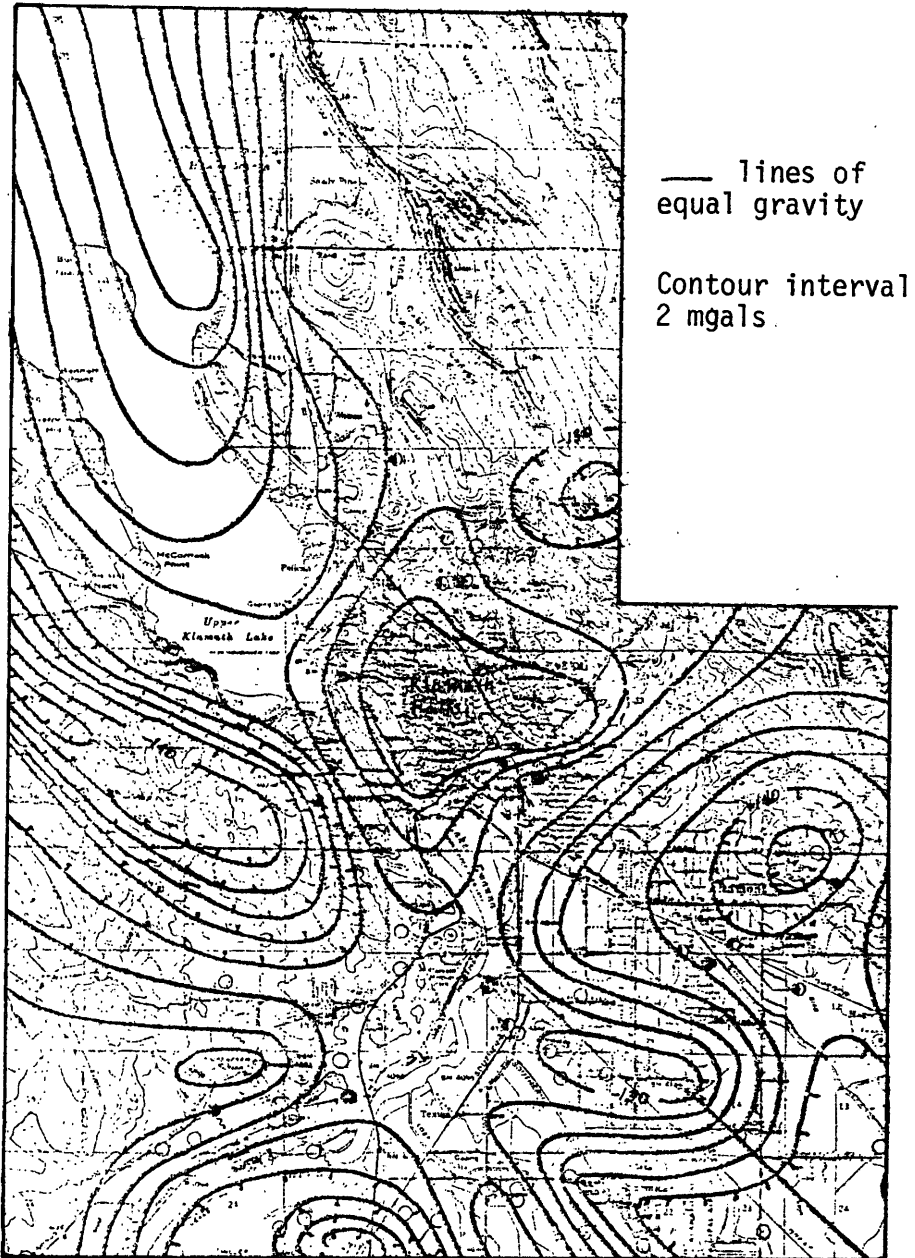
Figure 8. Gravity anomaly map of Klamath Falls area.
Note closed gravity high over Klamath Falls.
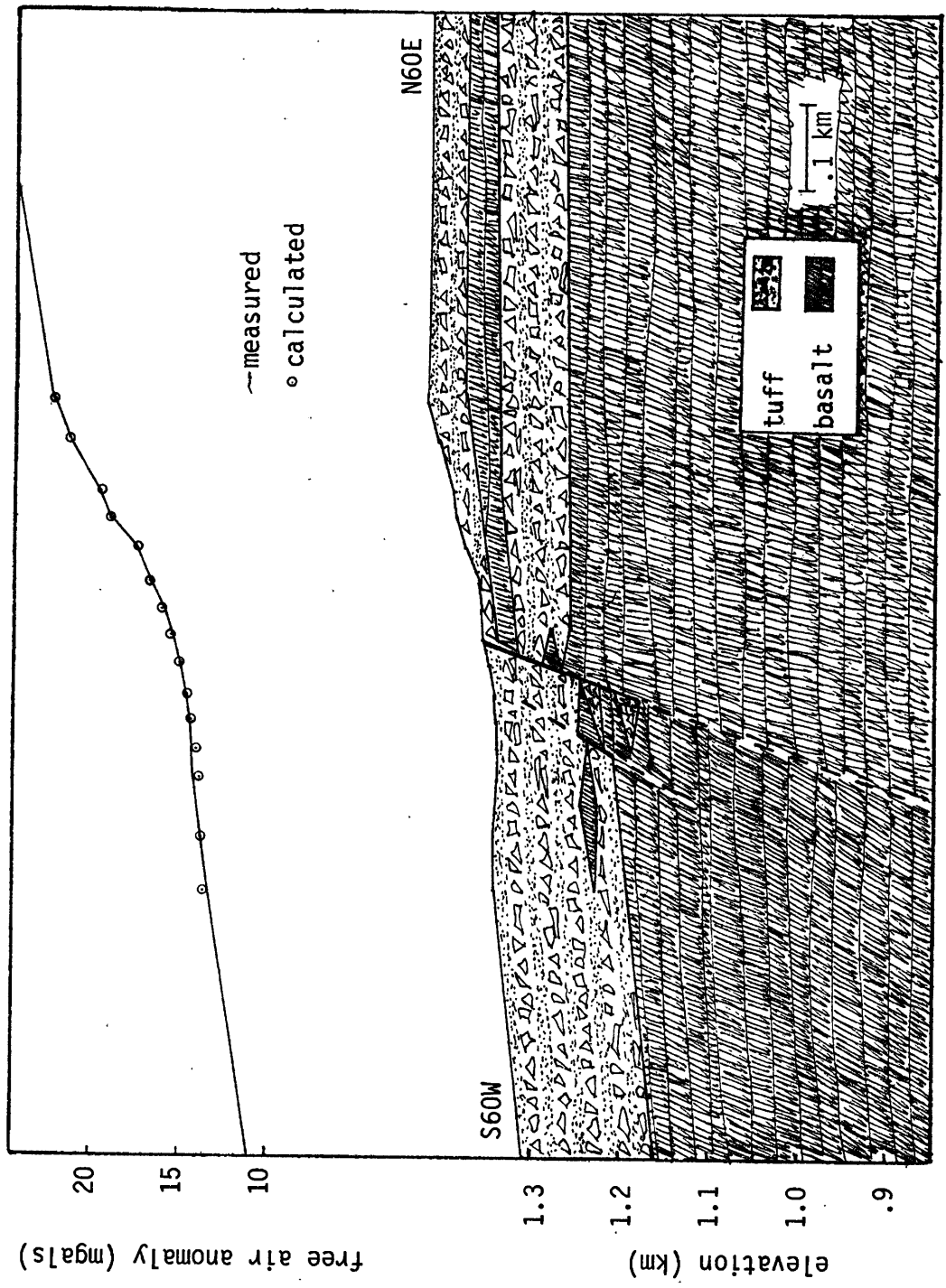
Figure 9.   Klamath Falls gravity line C - free air anomaly and associated model.

locations of basalts at the southwest end of line C. The thin beds of basalt on the southwest end of the line thin northward and are not present in the two gravity lines to the north.

Data from the three resistivity lines northeast of the fault (see Figure 16) were used in approximating depths to basalts. If a layer of rock was only a few meters thick, it was considered 'unnecessary' to the model and was not included. A lower layer of tuff, beneath the layer of basalt shown in the resistivity survey, was necessary to more closely match the calculated anomaly with the gravity profile. The position of this lower tuff is somewhat arbitrary - from well and outcrop data it was necessary that the tuff layers dip to the south and thin to the north, and placing the lower tuff layer in this location allowed it to be consistent with data from well number 1.

The fault in line C is located at the surface near gravity station 1 (see Figure 7). A model with a single fault was attempted at first, but later models contained a secondary fault to be consistent with the cross section. The distance between these two faults is approximately 45 to 75 m. A distance of approximately 65 m was used because is provided the best fit to the cross section.

Line B. Line B is located approximately 330 m north of Line C. The southwest end of the line is located near OIT dormitory buildings, and runs N60E just north of well number 1. The gravity profile and associated model are shown in Figure 10.

The downdropped side of the fault has a greater vertical displacement than in line C by approximately 50 m. This represents a slope of about eight degrees. The basalt layers present on the downdropped side
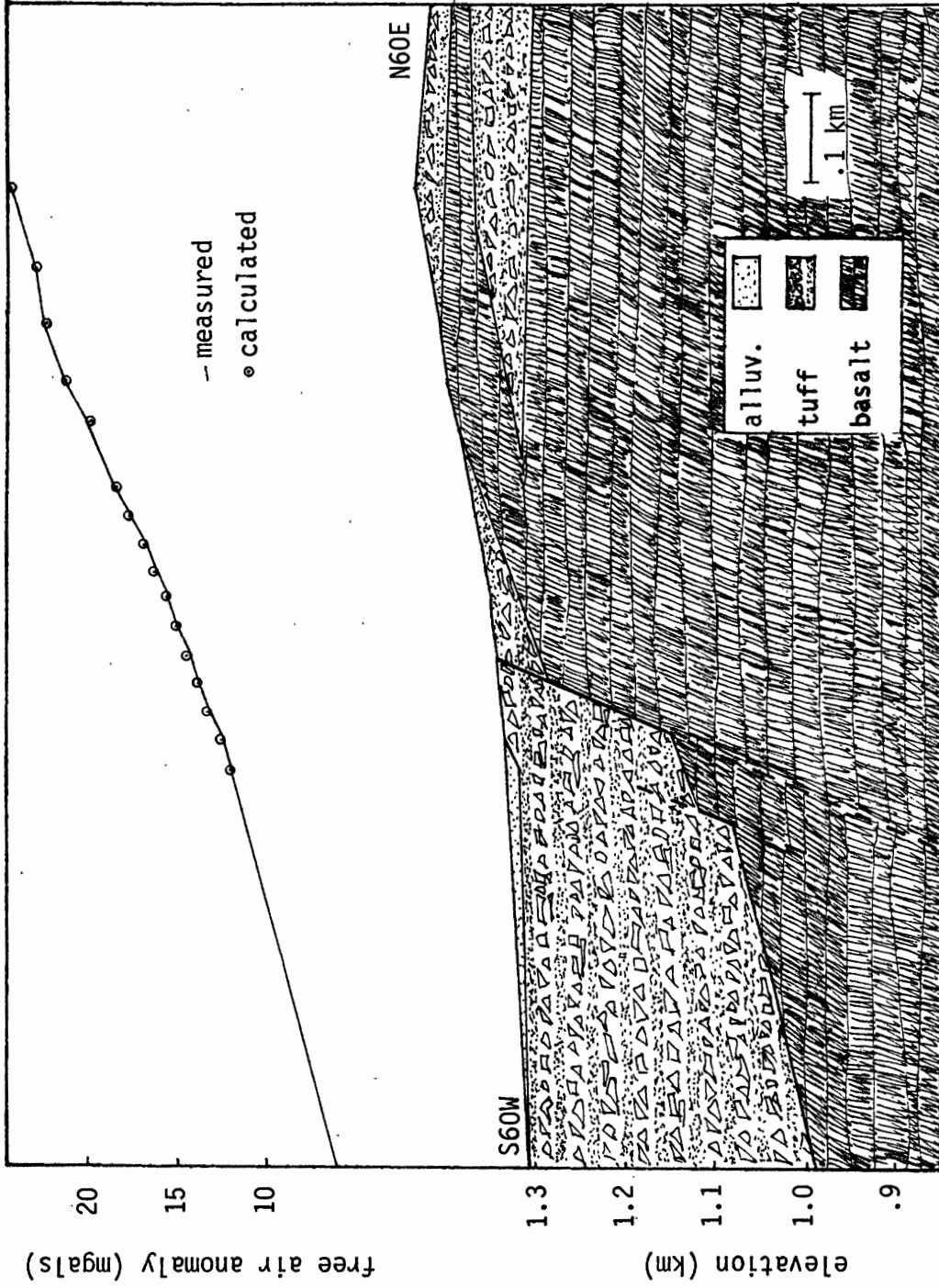
Figure 10. Klamath Falls gravity line B - free air anomaly and associated model.

of the fault on line C are not present in this line. From well data these basalts appear to thin out northward, and if they were to be included in line B, it would require that the southwest side of the fault be dropped down even more - to a dip that would seem less reasonable.

Outcrops along the hillside indicate a layer of tuff present, but data from well number 1 and outcrops of basalt near the northern water tank (see Figure 7) indicate that the tuff layer does not extend to the top of the hill, although more tuff crops out above the water tank. The 50 m of tuff near the fault was necessary to fit the gravity profile. The two layers of tuff on the northeast end of the line are the same layers as in line C, thinning out slightly, and dipping to the south. Well number 1, located near station 31, provided some control for a depth and thickness of the lower layer of tuff at that point. The surface location of the fault is near station 21, in a direction approximately N35W from its location on line 1.

Line A. Line A is the northernmost gravity line (see Figure 7). The profile and associated model are shown in Figure 11. The vertical displacement of the downdropped block is again, greater than the lines to the south, representing a slope of about twelve degrees, slightly greater than the slope between lines B and C. A surface density of 2.0 g/cc was used on the southwest end of the line for reasons explained previously. If this surface density was not used, and was assumed to be 2.4 g/cc, the calculated vertical displacement of the downdropped block would be even greater, resulting in an estimated slope of greater than twenty degrees, which seem unreasonable compared to the slope between lines B and C. The depth of the tuff layer immediately to the
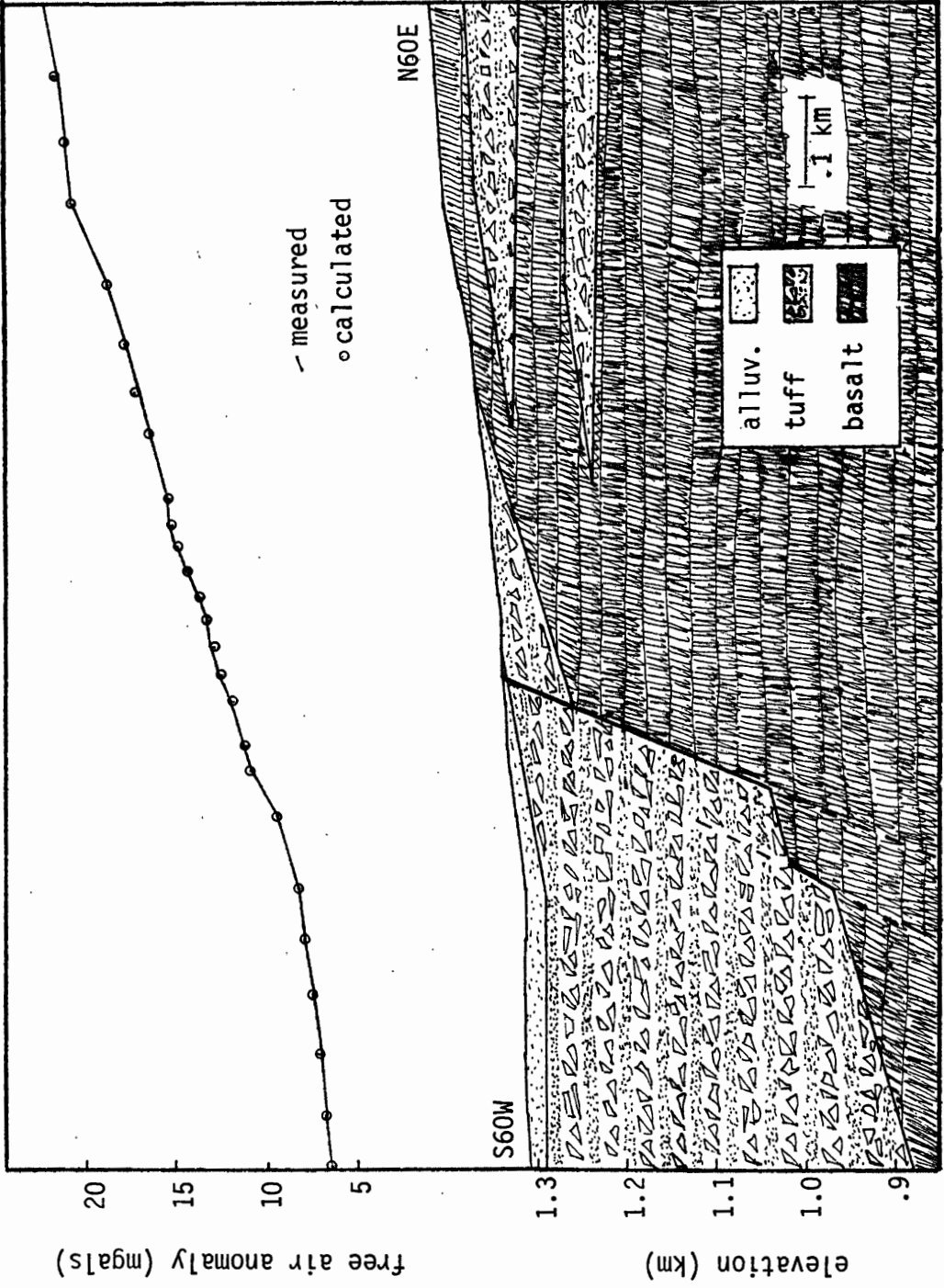
Figure 11. Klamath Falls gravity line A - free air anomaly and associated model.

northeast of the fault was determined from data from well number 3, located near station 42.

The upper tuff layer on the northeast end of the line is a continuation of the lower tuff layer on lines B and C. The upper layer of tuff in lines B and C is not present in this line, as basalt crops out along the hillside near the gravity stations. However, a second tuff layer not present in the other two lines was necessary to more closely match the calculated anomaly with the gravity profile. The surface position of the fault on this line is west of station 42 (see Figure 7).

After modelling was completed on these three lines, attempts at changing the position of the fault and its dip on line A were made to see the effects of these changes. Models of the fault with dips of 60 and 75 degrees were tried, but did not fit the gravity profile as well as an intermediate dip of 65 to 70 degrees. These models and profiles are shown in Figures 12 and 13. Models changing the position of the fault 10 m west and 10 m east on line A were also tried. Changing the position of the fault 10 m west appeared to work equally well, but changing the position 10 m east did not match the gravity profile as well. The gravity profiles and computed anomalies for these models are shown in Figures 14 and 15.

From the gravity modelling, the strike of the fault was fixed at approximately N35W. This differs slightly from the trend assumed for this study, N30W. The trend shown on the map is about N37W, but this is due to elevation changes. The fault dip is 65 to 70 degrees to the southwest. The calculated location of the fault in the study area is shown in Figure 7. Most of the curve in the trend of the fault near its
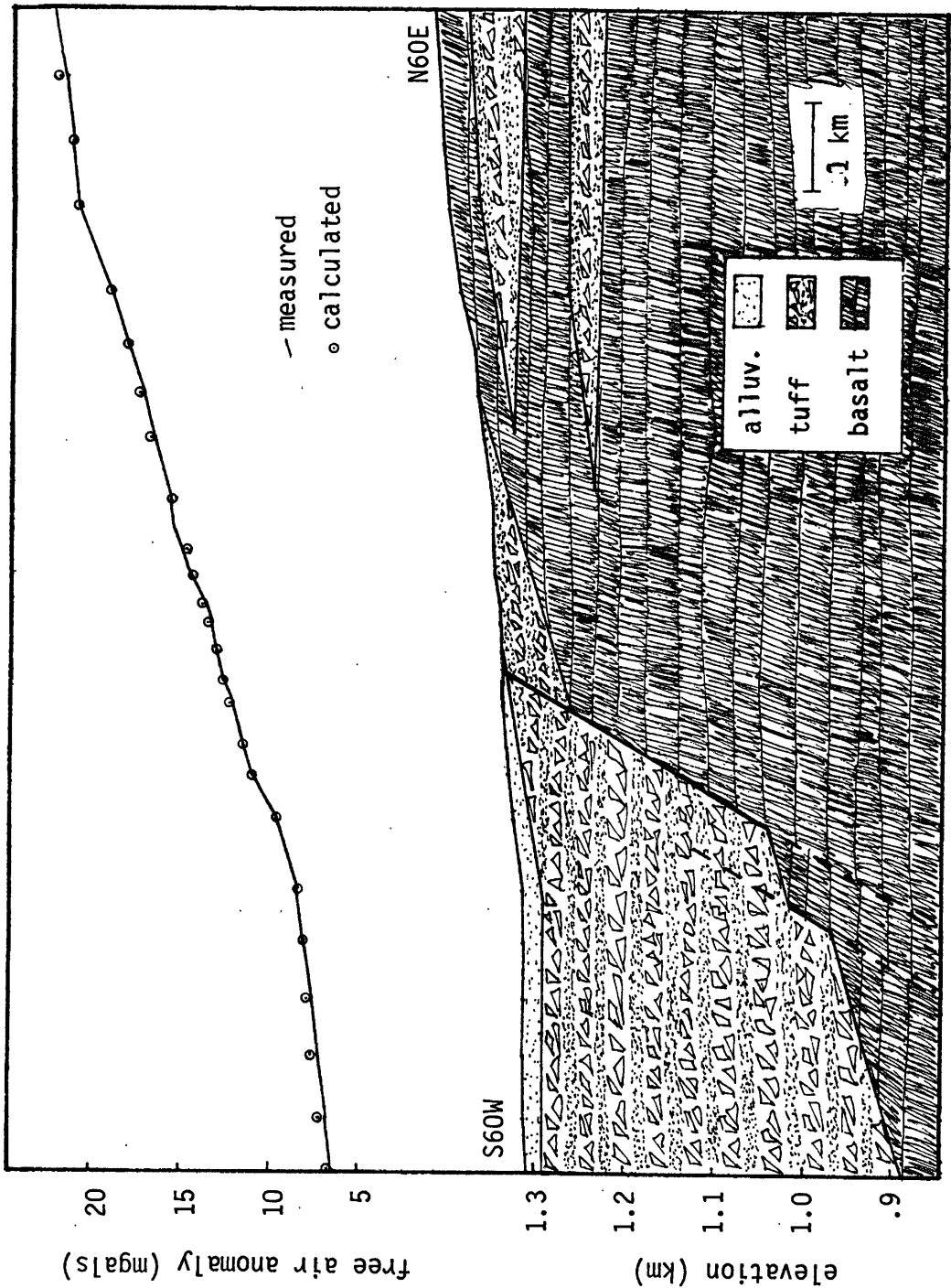
Figure 12. Klamath Falls gravity line A - free air anomaly and associated model for fault dip of 60° SW.

28
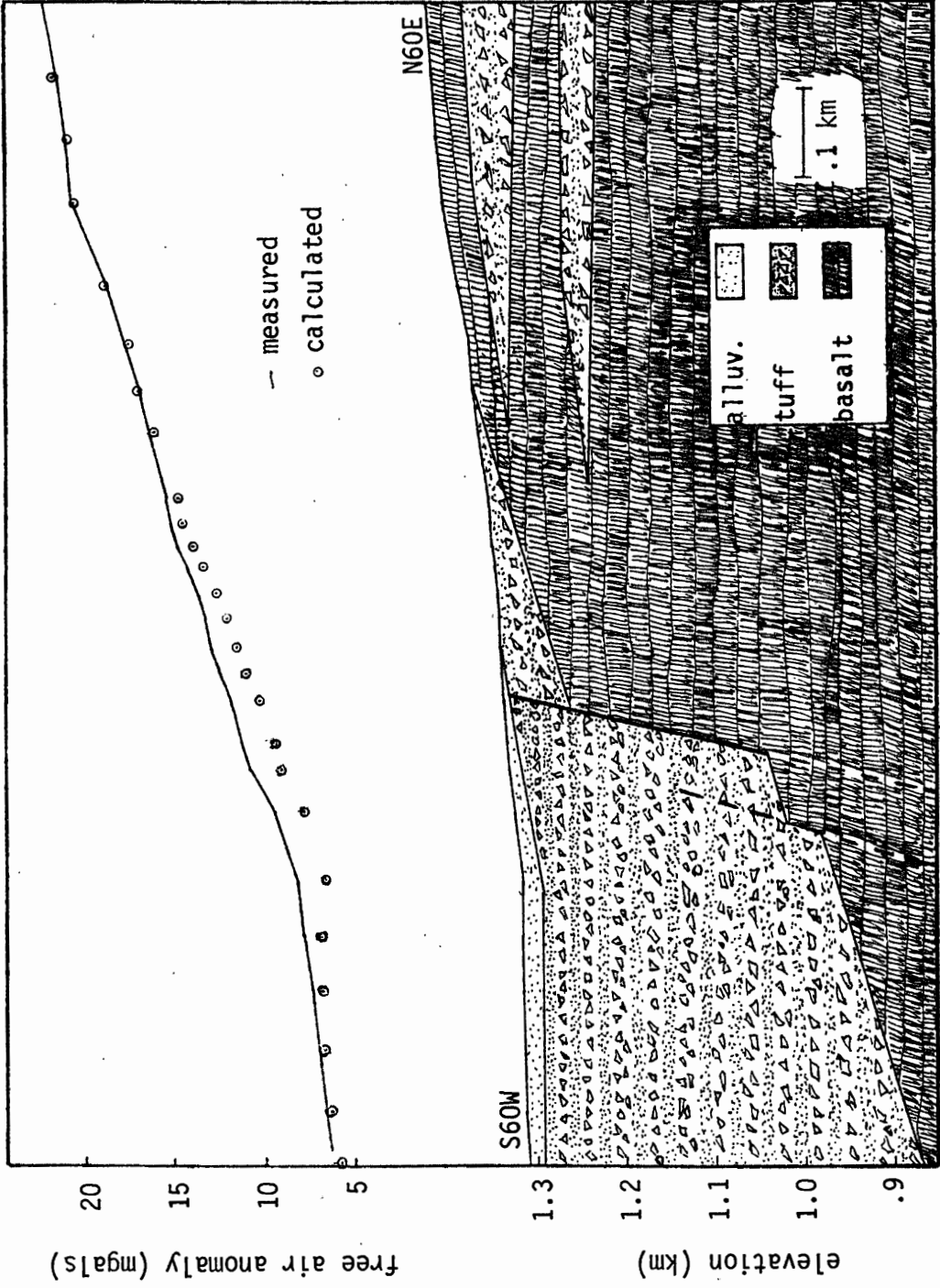
Figure 13. Klamath Falls gravity line A - free air anomaly and associated model for fault dip of 75° SW.
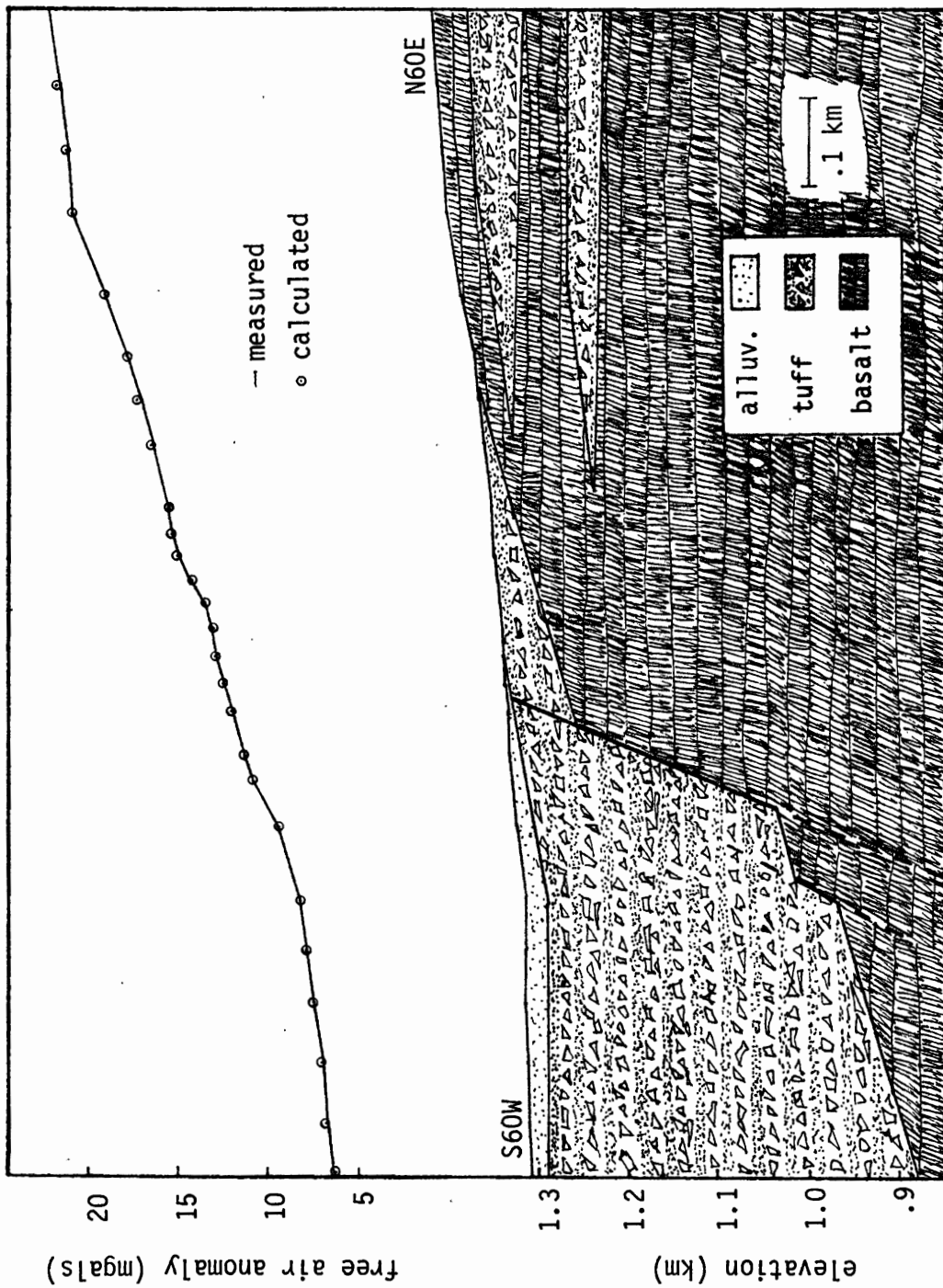
Figure 14. Klamath Falls gravity line A - free air anomaly and associated model for fault located 10 m west of calculated location.
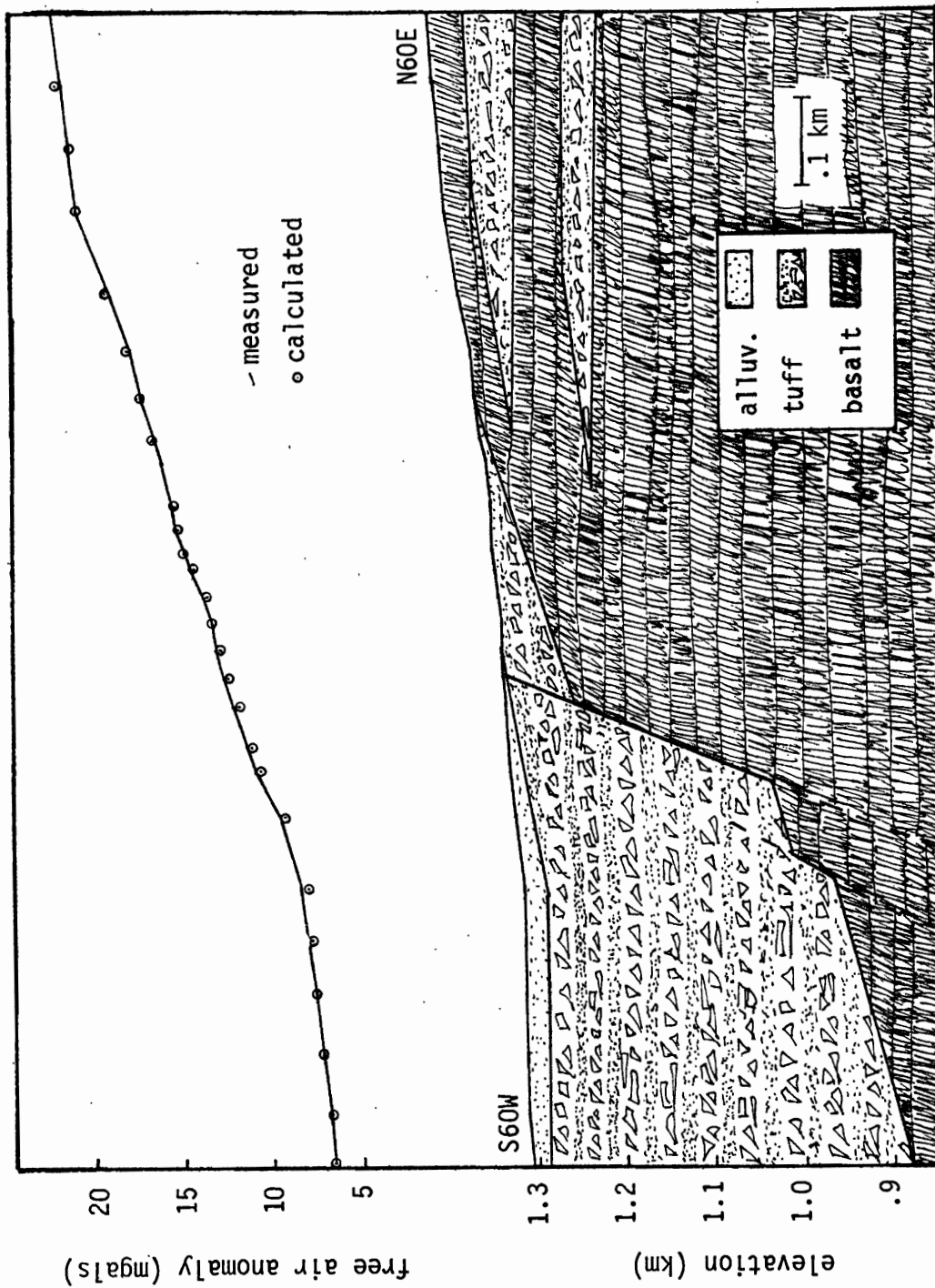
Figure 15. Klamath Falls gravity line A – free air anomaly and associated model for fault located 10 m east of calculated location.

exposure at the southern water tank (see Figure 7) is due to elevation change, but the fault itself may also curve slightly in this area. Vertical displacement on the fault increases from 100 m in the south to 200 m in the north. The position of the fault as located by gravity modelling is not exact, but probably varies by no more than 5 m on line C and 10 m on line A. The secondary fault is approximately 65 m west of the primary fault, and has a vertical offset of approximately 50 m.

RESISTIVITY

Resistivity provides a method of investigating bodies of rock based on their electrical characteristics. The resistivity is defined as the resistance of a cylinder with unit cross sectional area and unit length (Dobrin, 1976). For a cylinder of length 1, cross sectional area S, and resistance R, resistivity = RS/1, measured in ohm-meters. Resistivity may also be defined as the inverse of conductivity. The ease with which rocks conduct a current depends on the chemical composition of the rocks, the degree of compaction, the amount of water in the rock pores, and the amount of dissolved solids in the water.

The resistivity method involves placing four electrodes in the ground in one of several standard arrangements. An external voltage is applied across two of the electrodes, putting current into the ground, and the potential difference is measured across the other two electrodes. If the current lines pass through a homogeneous rock layer, the resistivity for that layer is directly measured. As the spacing between electrodes increases, so does the depth of penetration of the current flow lines, and increases the possibility that the flow lines will encounter another formation with a differing resistivity. The measured resistivity value will then be some combination of the resistivities of the upper lower units.

The type of information gained from the measurements is controlled by the spacing arrangements of the electrodes. In continuous profiling, the whole electrode array is moved along a line, and differences in

resistivity values reflect lateral variations in the rocks. In vertical sounding, the spacing between electrodes is progressively increased and vertical resistivity variations are seen. In the standard Wenner array (see Figure 17), often used in continuous profiling and vertical sounding, and the electrode setup used in this study, the depth of penetration of the flow lines is approximately equal to the distance between electrodes, or the a-spacing. In the Wenner arrangement, the apparent resistivity, or ρ_a, is equal to $2\pi aV/I$, where a is the a-spacing, V is the potential difference at the two inner electrodes, and I is the current put into the ground.

In areas where the water table is relatively shallow it is often difficult to obtain information other than the depth to the water table using resistivity methods. Low resistivity values are encountered at the water table because water containing dissolved solids is a good conductor, and other subsurface features tend to be hidden by the effects of the water table. Since the average annual precipitation in Klamath Falls is less than .365 m (15 in.), and the study was done in an area approximately 75 m above the level of Upper Klamath Lake, it was felt that subsurface features other than the water table could be detected.

Tuffaceous rocks in the Klamath Falls area are generally unfractured and non-porous. Little water can be contained in these rocks, and they have been assumed to have a high resistivity. Basaltic rocks in the area are highly fractured and thus have the ability to transfer water. Water in the area contains up to 900 mg/l dissolved solids (Sammel and Peterson, 1976), an amount which would significantly

increase conductivity, so the basalts have been assumed to have a rel-
atively low resistivity.

Field Work.

Five vertical sounding resistivity lines were run during June of
1979 in an attempt to determine depths to tuff and basalt layers which
might be used in gravity modelling. Three of the lines (1, 2, and 3)
were located on the northeast, or upthrown side of the fault, and two
(4 and 5) were located on the southwest, or downthrown side of the
fault (Figure 16).

An Atlas Copco ABEM Terrimeter was used in a standard Wenner array
in the survey. The spacing between electrodes was expanded from 1.5 to
3, 6, 15, 30.5, 61, and 152 m as needed. If the resistivity values re-
mained constant over several a-spacings and were not expected to change,
the array was only expanded to an a-spacing of 61 m. The readings on
the Atlas Terrimeter are values of V/I times some power of ten. To
find the apparent resistivity, this value was multiplied by the multi-
plication factor and then $2\pi a$, where a was the a-spacing.

Interpretation.

The Tagg method for interpreting simple two or three horizontal
layer cases was used on the resistivity data (Dobrin, 1960). Tagg
curves are a family of k curves plotted on a ρ_a/ρ_1 versus h/a graph,
shown in Figure 18. H is the depth to discontinuity and k is the resis-
tivity contrast. Since the apparent resistivity is the measured quanti-
ty, then a-spacing versus apparent resistivity for various a-spacings
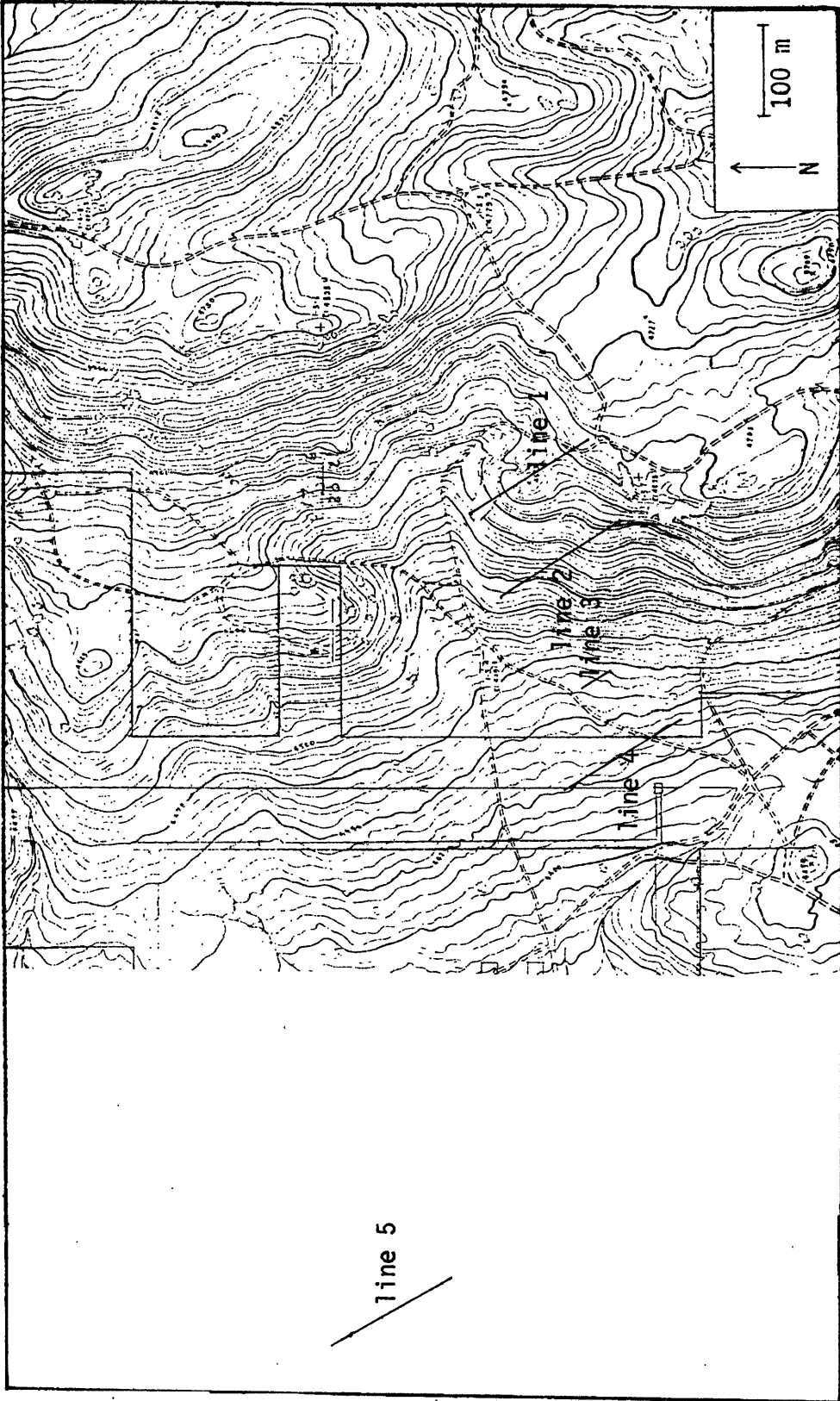
Figure 16. Location of five resistivity lines.
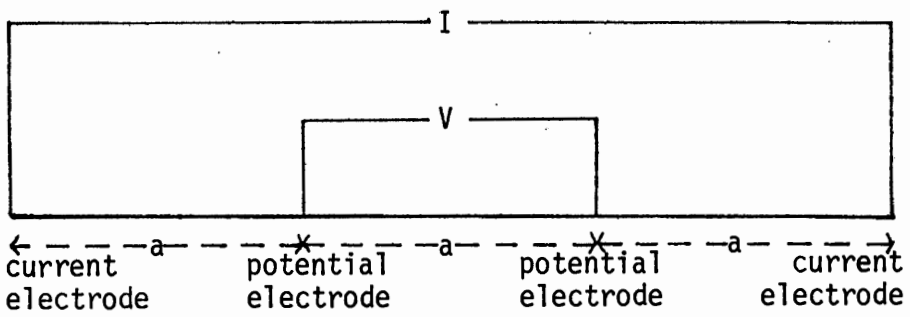
Figure 17. Standard Wenner electrode array used in resistivity survey (Dobrin, 1976).
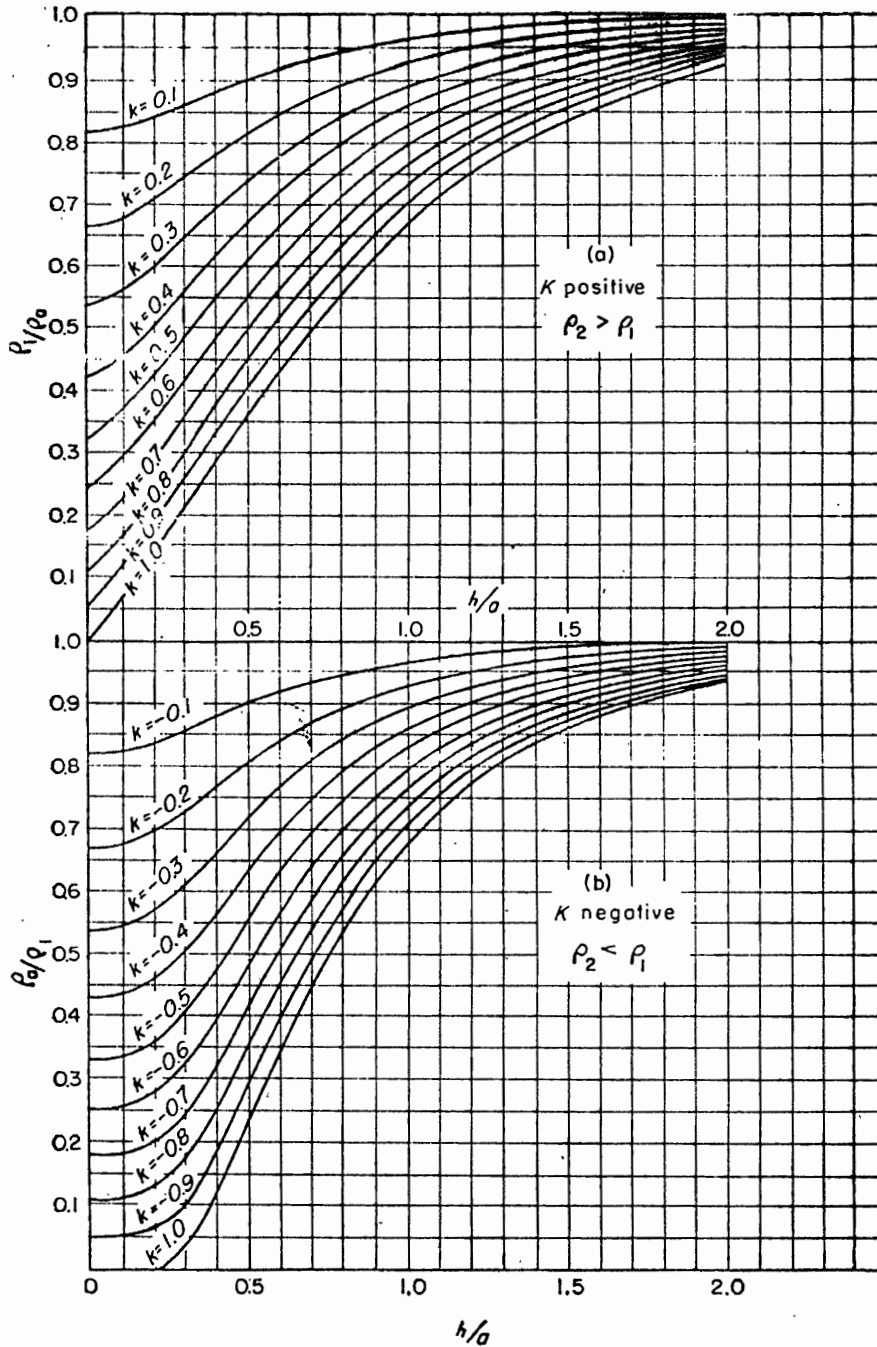
Figure 18. Tagg curve used in computing depth to interface from resistivity data (Dobrin, 1960).

can be matched with the theoretical Tagg curves to give values or h and k. The ρ_a/ρ_1 value for field data is found by estimating ρ_1 from ρ_a at values of a that approach zero and dividing the ρ_a value for each a-spacing by this value of ρ_1. These values are then plotted as horizontal lines on the Tagg curve graph of ρ_a/ρ_1 or ρ_1/ρ_a (whichever value is less than one) versus h/a. A plot of k versus h is developed, giving a curve for each a-spacing, and where these curves intersect, the value for h at that point is taken to be the depth to the second layer.

Line 1. Line 1 is located on the upthrown side of the fault. Plots of apparent resistivity versus a-spacing and k versus h for line 1 are shown in Figure 19. An isolated basalt outcrop near the line was interpreted to be only a thin cap, and the Tagg curve intersection at 2 m was taken to be the depth to a tuff layer below the basalt. This was consistent with the high resistivity values for a-spacings from 6 to 61 m. Another Tagg curve intersection at approximately 44 m was interpreted to be the depth to a basalt layer below the tuff. This corresponded with low resistivity at a-spacings of 61 and 152 m.

Line 2. Line 2 is located northeast of the fault, shown in Figure 16. The same pattern in the apparent resistivity versus a-spacing plot of line 1 is evident in line 2 - low resistivity values at small a-spacings, high resistivity at intermediate a-spacings, and low resistivity values at greater a-spacings (Figure 20). However, the gradual increase of resistivity at a-spacings of 61 and 152 m is somewhat confusing. It is possible the basalt is compressed depth, and some of the fractures are closed, closing water channels. If this is the case, it
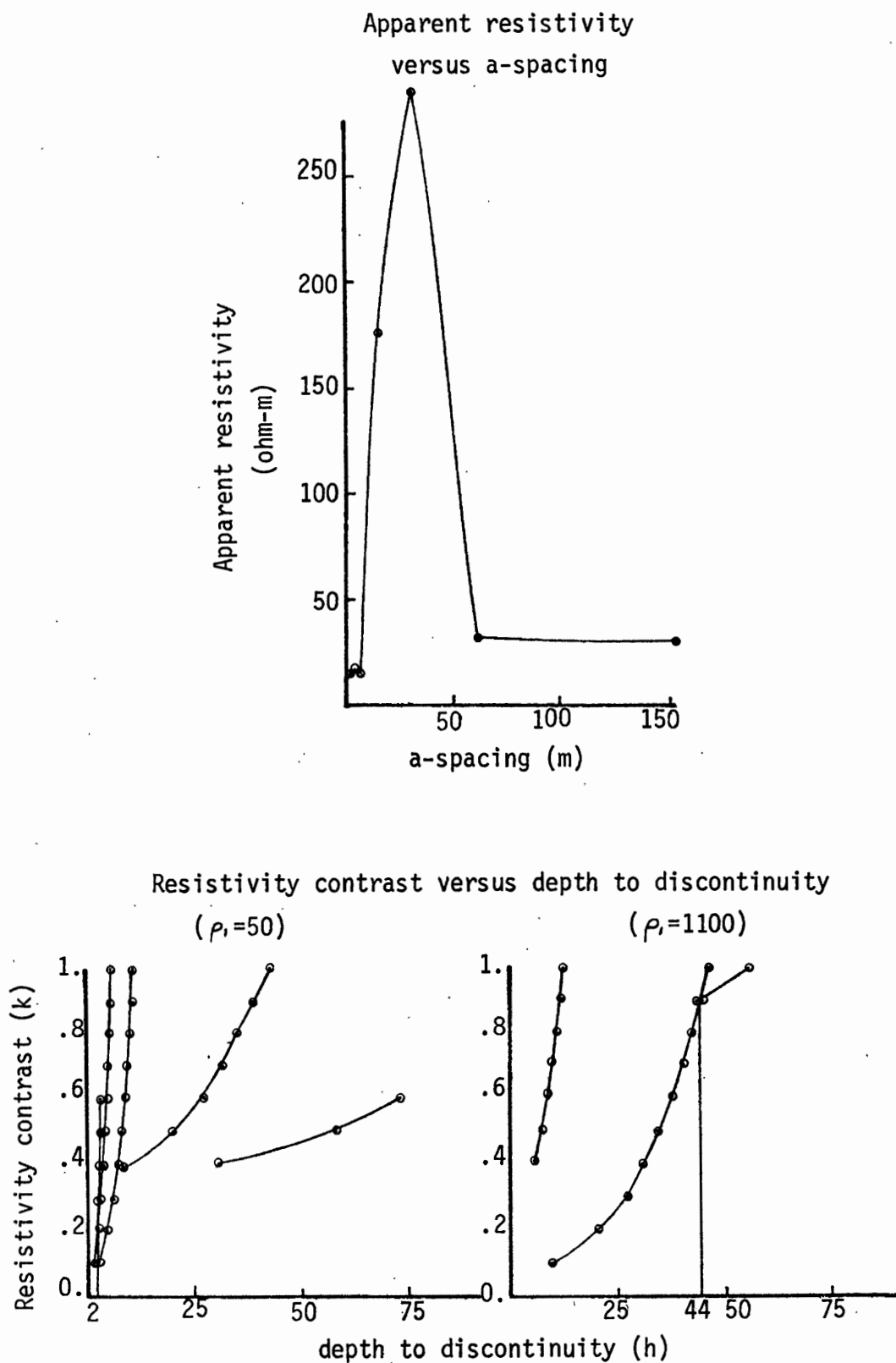
Figure 19. Plot of apparent resistivity and k versus h for resistivity line 1. Intersections on lower graph are depths of discontinuity.

Apparent resistivity
versus a-spacing

Resistivity contrast versus
depth to discontinuity (ρ_1=55)
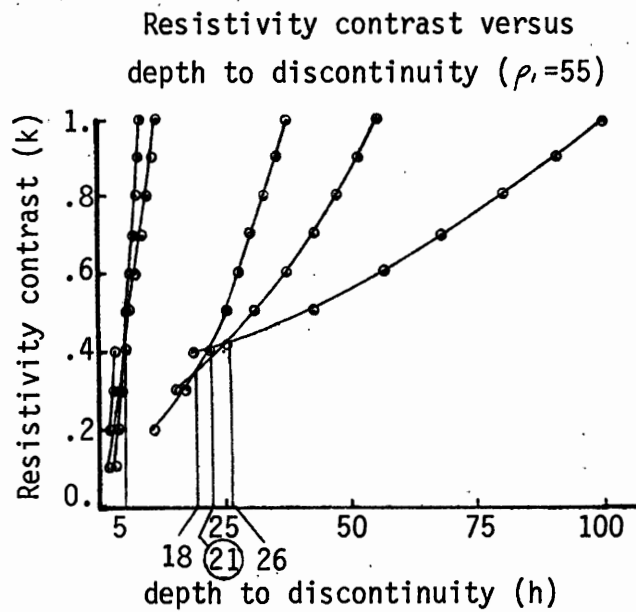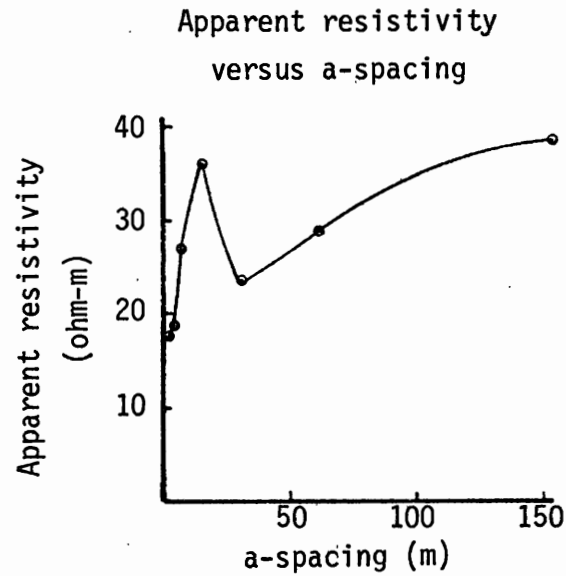
Figure 20. Plot of apparent resistivity and
k versus h for resistivity line 2.

is curious that other lines did not indicate the same pattern. Tagg curve intersections occurred at 5 and 21 m. Five meters was taken to be the depth to the tuff layer. Twenty-one meters was interpreted to be an approximate depth to the lower basalt layer.

Line 3. Line 3, just northeast of the fault, (Figure 16), showed a high resistivity layer at small a-spacings and a lower resistivity layer at greater a-spacings. The one point low resistivity value at 3 m spacing may be due to a very thin finger of basalt. Plots of k versus h (Figure 21) show depths of 1 m and 11 m to interfaces. The 1 m interface was interpreted to be the thin basalt wedge, and the 11 m intersection has been interpreted to be the depth to a lower basalt layer.

Line 4. Line 4 was run on the downthrown side of the fault near two of the hot water wells and an OIT heat exchange building (Figure 16). The plot of apparent resistivity versus a-spacing is shown in Figure 22, along with the plots of k versus h for this line. If the line lies below the fault, then the depth to which the a-spacing permits penetration should show only a high resistivity layer, tuff, to be consistent with well data from the area. A Tagg curve intersection of 3 to 6 m may be due to water flow in the surface layer due to the three hot water wells in the area, or to interference with underground pipes from the heat exchange building.

Line 5. Line 5 was located on the downthrown side of the fault west of the OIT campus. The lowest resistivity value was measured at 152 m a-spacing. Plots of k versus h (Figure 23) showed an
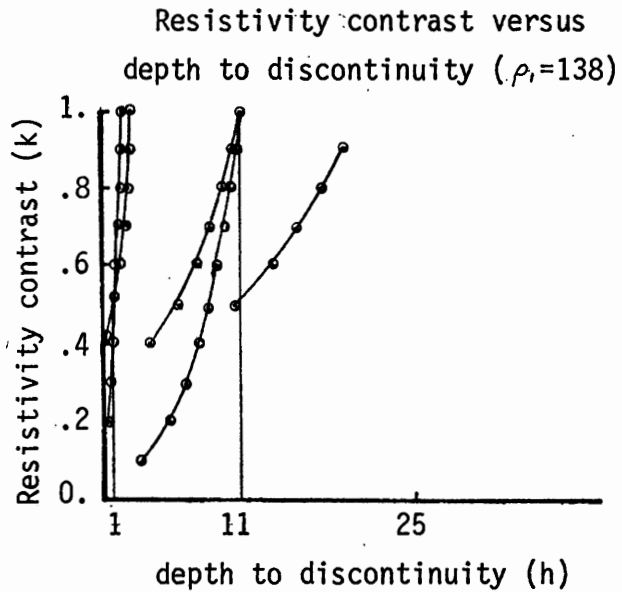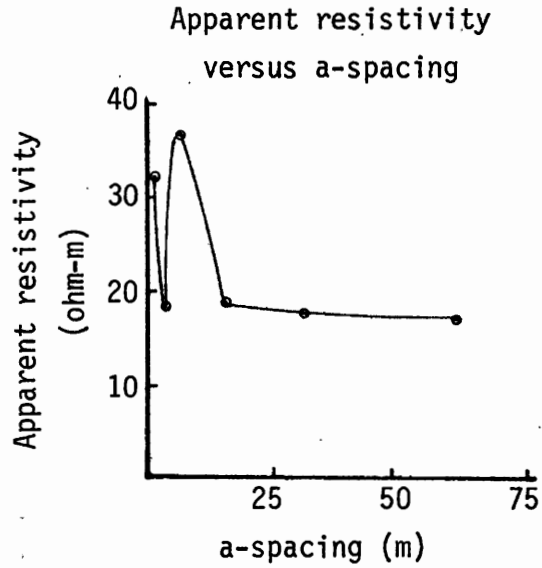
Figure 21. Plot of apparent resistivity and k versus h for resistivity line 3.
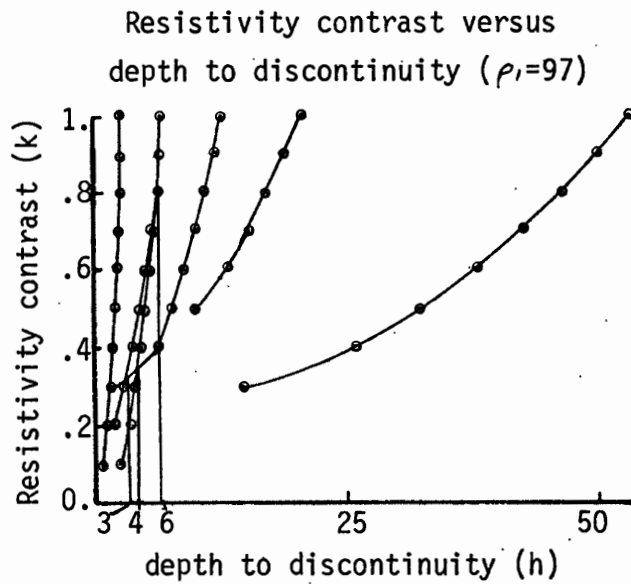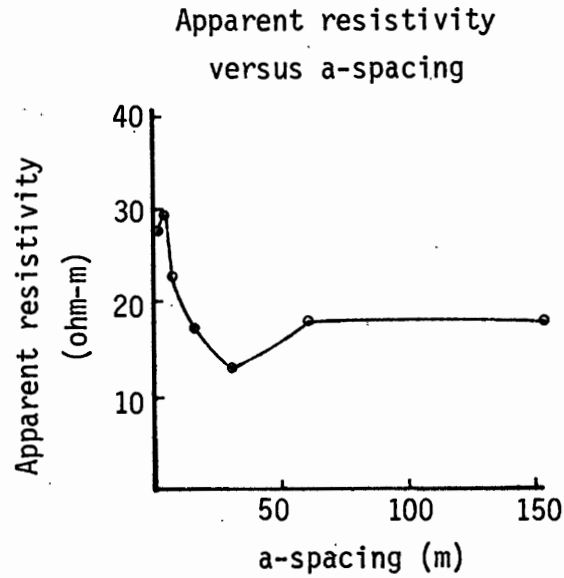
Figure 22. Plot of apparent resistivity and k versus h for resistivity line 4.

Apparent resistivity
versus a-spacing

Resistivity contrast versus
depth to discontinuity (ρ_i=7)
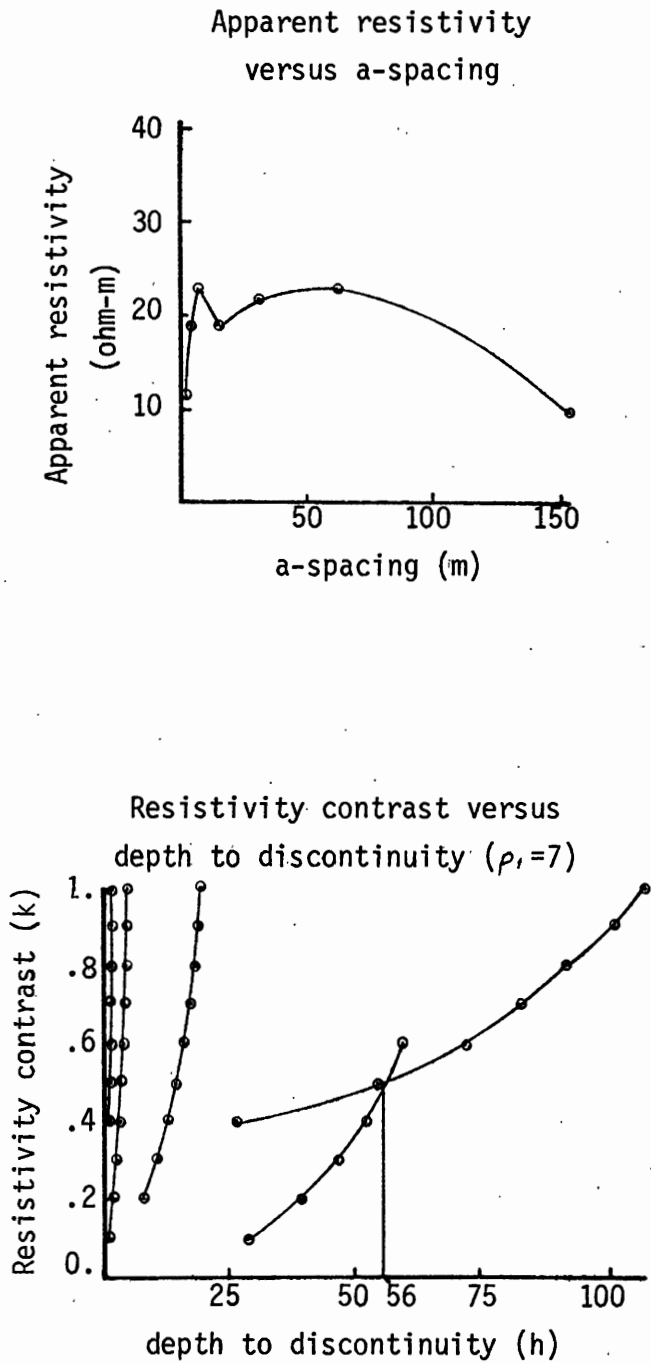
Figure 23. Plot of apparent resistivity and
k versus h for resistivity line 5.

intersection at approximately 56 m. Klamath Lake lies approximately 61 m below the elevation of this line, so this 56 m intersection was taken to be the depth of the water table in this area.

The calculated depths to basalt and tuff layers were used where possible in the gravity modelling. Data from lines 1, 2, and 3 were used in determining depths to a basalt layer in the model for gravity line C. Line 4 showed an interface which may be due to interference from water wells and pipes in the area, and line 5 showed an interface interpreted to be the water table in the area. A cross section perpendicular to the resistivity lines using depths calculated from the plots of k versus h is shown in Figure 24.
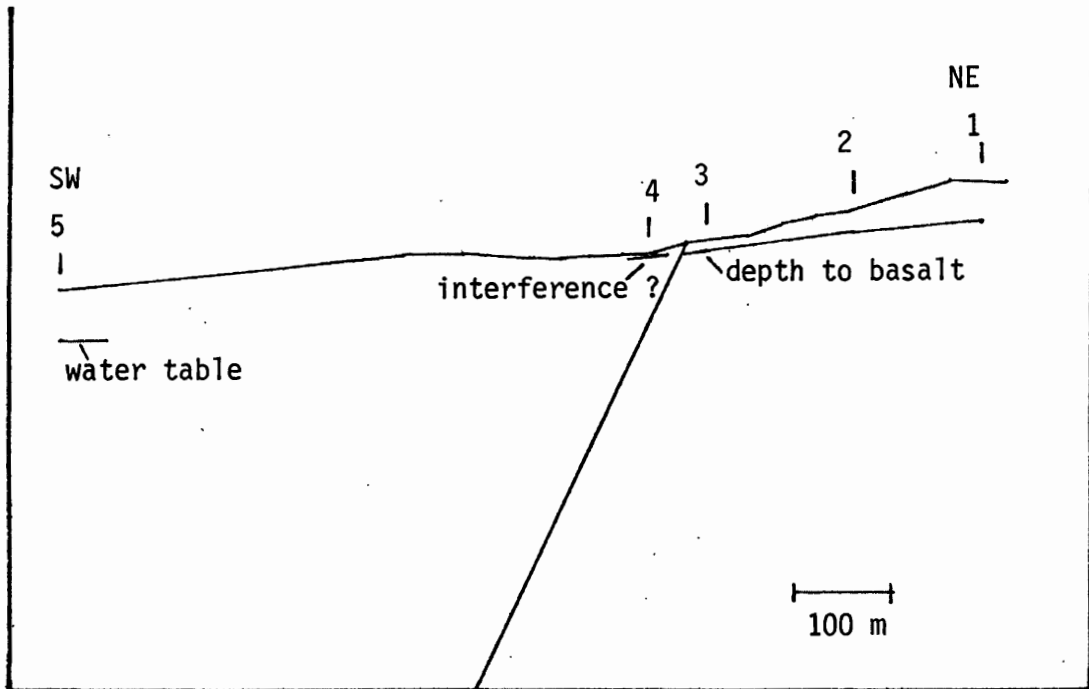
Figure 24. Cross section perpendicular to resistivity profiles.

SEISMIC REFRACTION

Seismic exploration depends on the propagation of waves through elastic media. An elastic substance is one which deforms when a force is applied but returns when the force is removed. Rocks can be considered to be elastic if deformations are small. The velocities at which seismic waves travel through rocks depend on the density and elastic properties of the rock units.

Relations between stress and strain are defined by certain elastic constants. Young's modulus (E) measures the relation of compressional or tensional stress to linear strain: $S = E \partial u / \partial x$, where $\partial u / \partial x$ is the change in length in the x direction. The bulk modulus, k, measures the proportionality between hydrostatic pressure and cubic dilitation, and is equal to $P/(\Delta V/V)$, where P is hydrostatic pressure, ΔV is the change in volume, and V is the original volume. The rigidity modulus, μ, relates shear stress to shear strain in the equation $S_t = \mu \varepsilon$. Poisson's ratio, σ, is the change in length of one dimension of a body due to a change in length in another dimension.

When stress is applied to a body, the resultant strain is propagated outward as waves. Surface waves travel across the free surface of an elastic body, while body waves travel within the body. There are two types of body waves. P waves are compressional-dilitational waves which cause a change in only the volume of a material. Particle movement is in the direction of travel. Shear waves, or S waves, cause a rotation in the material. Particles move perpendicular to the direction

of wave propagation. The velocity of P waves in rocks is given by the equation: $V_p=\sqrt{(k+4\mu/3)/\rho}$ or $\sqrt{(1-\sigma)E/(1+\sigma)(1-2\sigma)\rho}$ where ρ is the rock density. The shear wave velocity, V_s is $\sqrt{\mu/\rho}$ or $\sqrt{(E/\rho)(1/2(1+\sigma))}$. For most rocks, $\sigma=.25$, and V_p is then approximately 1.7 times V_s.

When a stress is applied at a point, P and S waves travel in all directions. As the waves strike an interface, part of the wave energy is reflected, and part of the energy is refracted into the second medium. The angle at which the refracted wave travels in the second medium is given by the relation: $\sin a/\sin R_p=V_{p1}/V_{p2}$, Snell's law. V_{p1} is the P velocity in the upper layer, V_{p2} is the P velocity of the second layer, i is the angle of incidence, and R_p is the angle is refraction of the P wave. If sin i is equal to V_{p1}/V_{p2}, then sin R_p is equal to one, R_p=90 degrees, and the refracted wave travels along the interface. The critical angle, i_c, equal to $\sin^{-1}(V_{p1}/V_{p2})$, is the angle necessary for this refraction to occur. Energy is also refracted back towards the surface at the critical angle. For refraction at the critical angle to occur, V_{p1} must be < V_{p2}. Low speed layers underlying higher speed layers are not 'seen' as refractors in seismic refraction.

In a refraction survey, a series of geophones is placed along a line. A seismic wave is generated at one end of the line, and the time of arrival of the refracted wave at each geophone is recorded (Figure 25). These times are used in calculating depths to interfaces and velocities.

Refraction lines are reversed (the wave is generated at the opposite end of the line) to check for dipping beds. The time for the wave
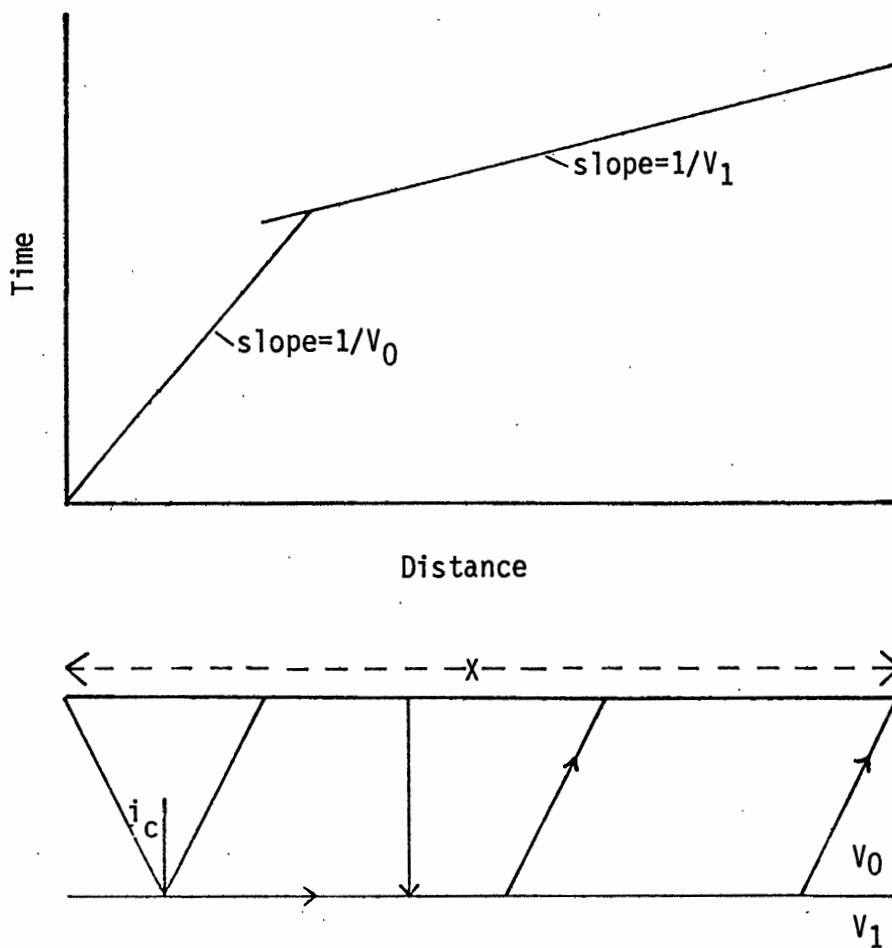
Figure 25. Refraction profile (top) for horizontal beds with velocities V_0 and V_1 (Dobrin, 1976).

to travel the total distance is the same, but if the beds are dipping, it will take longer for a wave introduced at the downdip end of the line to reach an intermediate geophone than one introduced at the updip end of the line (Figure 26).

Surface velocities for the area were estimated to be between 200 and 700 m/sec, velocities for a soil-sand-clay mixture (Clark, 1966) Tuff velocities were estimated to be between 1500 and 2500 m/sec (Clark, 1966). Basalt velocity was estimated to be approximately 5000 m/sec. This is a rather low velocity for basalt (range of 5000-6400 m/sec: Clark, 1966) but was thought appropriate for the fractured basalts of the area.

Field Work.

The refraction survey was carried out in June, 1979. Three lines were run: one northeast of the fault, one southwest of the fault, and one across the fault (Figure 27).

Lines were 335 m (1100 ft.) in length. Twelve geophones were placed in a line at approximately 3 m and 15 m spacing from the point of the weight drop. The closer spacing was used to estimate surface velocities. The recording equipment, consisting of a power source, an amplifier, and an oscillograph, and carried in a separate vehicle, was left at either end of the line. Three drops were completed for each forward and reverse line: a 3 m spacing drop, a 15 m spacing drop covering the first half of the line, and a 15 m spacing drop covering the second half of the line. All lines were reversed. A thumper (a weight-dropping device), loaned by the School of Oceanography, Oregon State University,
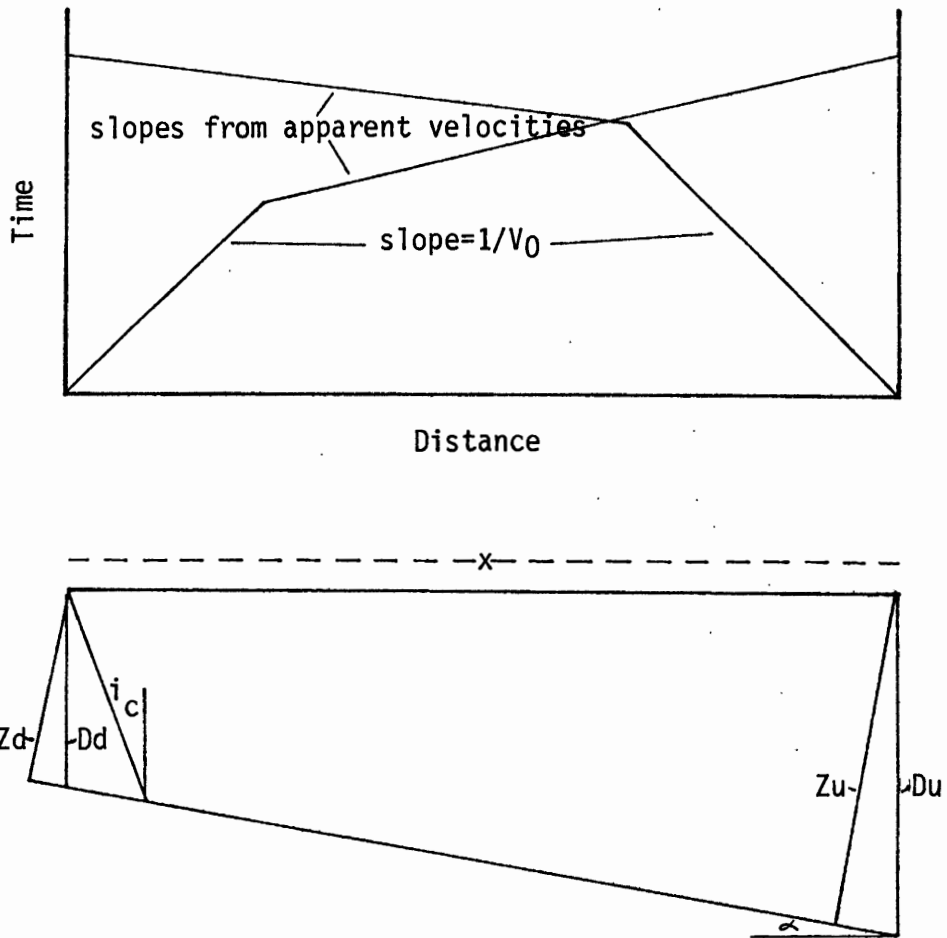
Figure 26.   Refraction profiles for bed dipping at angle α (Dobrin, 1976).
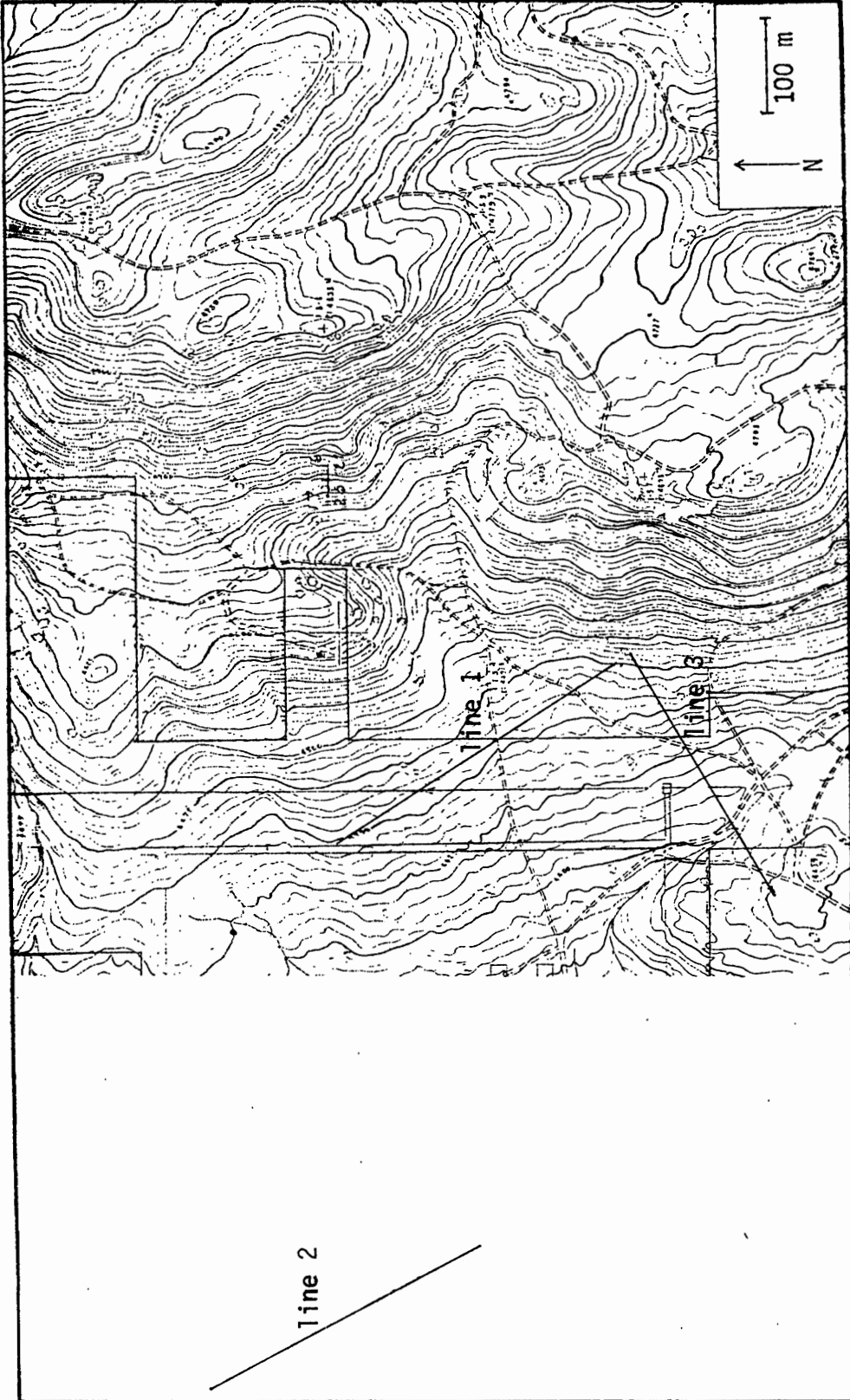
Figure 27. Location of refraction lines.

was used to generate a seiamic wave. The drop was repeated until the
arrival time at each geophone was recorded clearly. Gain and filter
adjustments on the amplifier were used to adjust the signal and noise
levels. When the first half of the line at 15 m spacing was completed,
the last geophone was left in place and the other geophones were placed
at 15 m spacing along the second half of the line. When the second for-
ward profile was complete, the process was reversed to check for dipping
beds.

Interpretation.

Arrival times for refracted waves were plotted on time versus
distance graphs, and velocities of layers calculated by a least squares
method (Walpole and Meyers, 1978). Depths to interfaces and dip angles
of beds were calculated using methods in Dobrin (1976, pp. 296-305).

Because the refraction survey was conducted after gravity model-
ling was completed, the refraction data was used as a gravity model
check. Calculated depths to interfaces were not always exactly the
same as those used in the gravity modelling, but there is enough un-
certainty in the methods to imply that all differences may not be real.

Line 1. Line 1, located just northeast of the fault, is shown in
Figure 27. The forward and reversed profiles show three layers (Figure
28). The surface layer has an average velocity of 435 m/sec (1400 ft./
sec), and a calculated depth of approximately 12 m. The layer dips to
the south at approximately 2 degrees, almost negligible. A surface
density was not used in the modelling of gravity lines A and B, located
near the ends of refraction line 1. A surface layer with density of
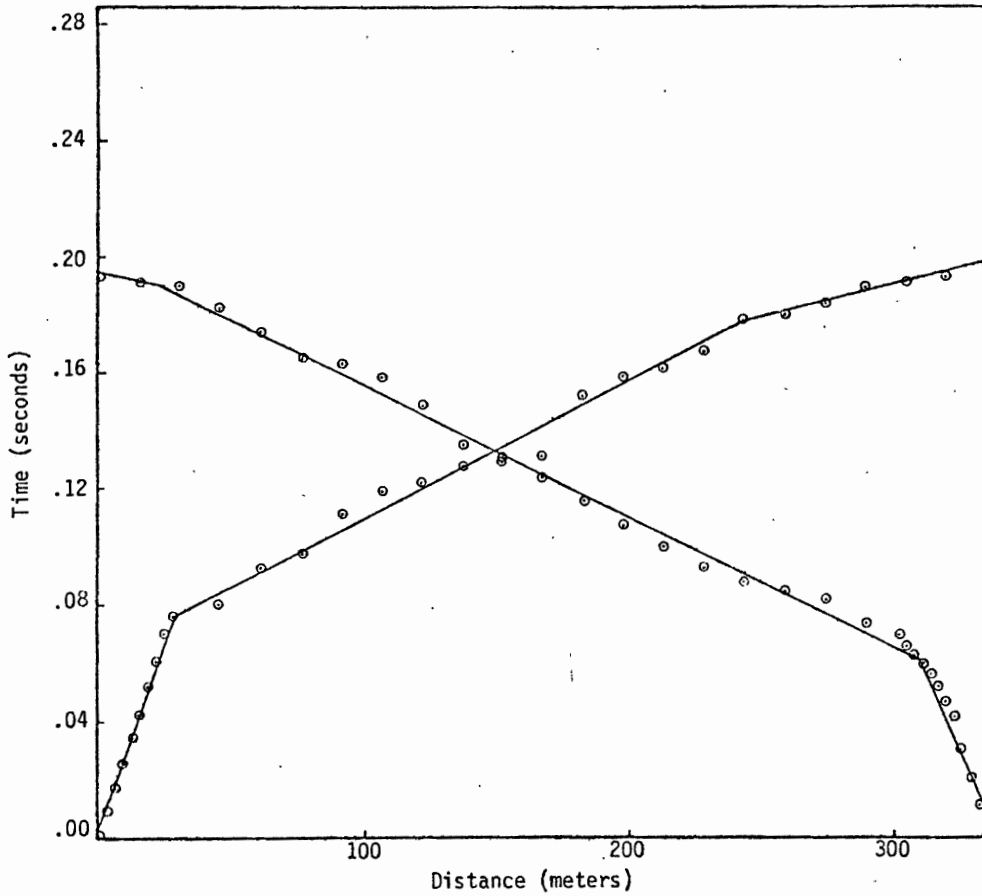
Figure 28. Refraction profile for line 1, northeast of fault.

2.0 g/cc 12 m thick would change the gravity by approximately .2 mgal.
If the surface density were used on both sides of the fault, the loca-
tion of the fault would not change.

The velocity of the tuff was calculated to be approximately 2175
m/sec (7140 ft./sec). Calculated basalt velocity is approximately 4800
m/sec (15,750 ft./sec), which is lower than estimated, but not unrea-
sonable for fractured basalts. The depth to the basalt-tuff interface
was calculated to be approximately 85 m (280 ft.) at the north end of
the line, and 95 m (315 ft.) at the south end. If the length of the
line and the elevation difference between the ends of the line are taken
into account, the dip is negligible.

The difference between the depth to the basalt in this area used
in the modelling of gravity line B and the depth calculated at the north
end of the refraction line is approximately 15 m. The gravity model in
this area was constrained by data from well number 1, and 15 m is not
an unreasonable difference considering error in both methods.

The calculated depth to the basalt at the south end of the line
is approximately 95 m. This does not agree at all with the depth to
the upper basalt layer in the area used in gravity line C. However,
the depth to the lower basalt layer is approximately 90 m, which agrees
quite well with the refraction data. This discrepancy may be explained
if the tuff layer just north of the fault in gravity line B (Figure 10)
meets both tuff layers north of the fault in gravity line C (Figure 9).
The refracted wave might travel along the interface connected by these
layers. Two cross sections of possible subsurface structures parallel
to the fault are shown in Figure 29. The upper basalt layer in gravity
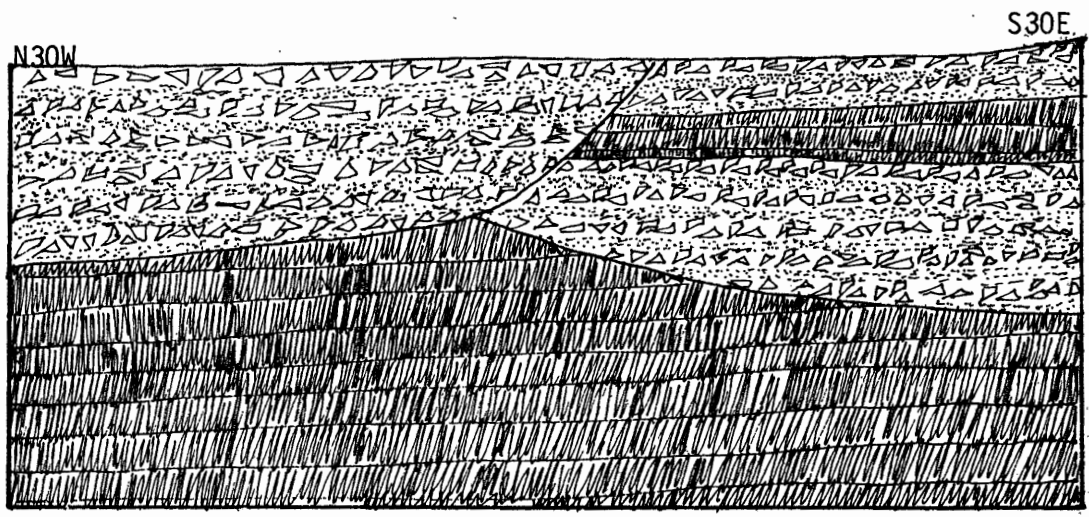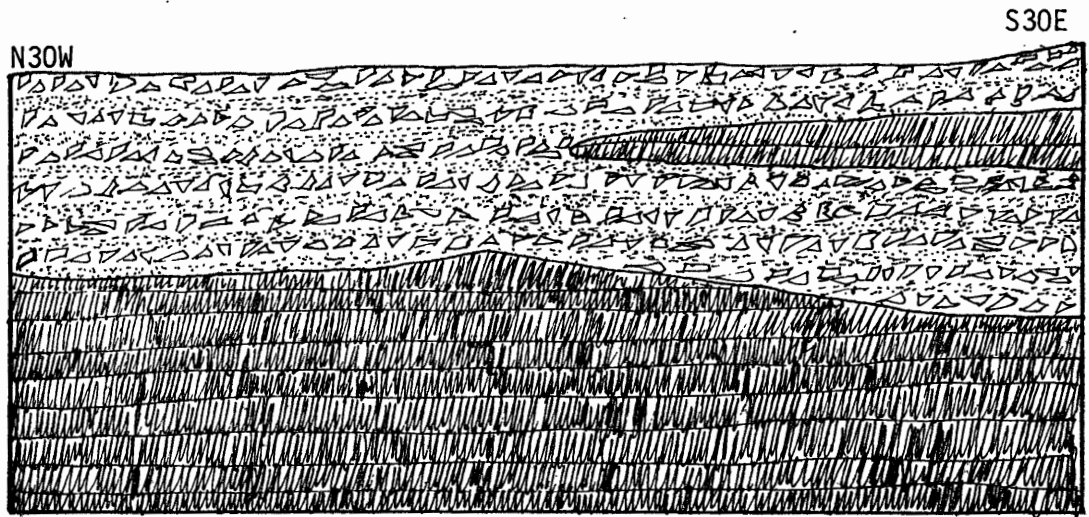
Figure 29. Models of possible subsurface structure along refraction line 1.

line C may either thin out to the north, or be truncated by erosion.

Line 2. Line 2 is located southwest of the fault near the end of gravity line A (Figure 7). This is the area in which resistivity line 5 was run. The refraction profile (Figure 30) shows two layers. The profile is characteristic for a dipping bed, giving two apparent velocities for the lower layer. The velocity of the upper layer is approximately 600 m/sec (1975 ft./sec). This bed dips to the north at an angle of 5.5 degrees. Its depth at the south end of the line is less than a meter; near the north end of the line its depth is approximately 25 m. This is consistent with the 2.0 g/cc density layer used in gravity lines A and B. The thickness of the layer is near zero at the southwest end of gravity line B, and thickens to approximately 20 m at the southwest end of gravity line A, with a dip of approximately 3.5 degrees. The lower layer has a velocity of approximately 1482 m/sec (4860 ft./sec), and was interpreted to be tuff.

Line 3. Line 3 was run across the fault, near the location of gravity line A. The refraction profile is shown in Figure 31. It was hoped that this line would show a standard normal fault profile, (Figure 32, Sharma, 1976), but this was not the case. Results for the second half of the forward drop were not obtainable. Even with adjusting the gains and filters of the geophones on several drops, no clear wave arrivals could be seen. The profile does show two layers - the surface layer has a velocity of 690 m/sec (4850 ft./sec). The calculated depth of this layer on both ends of the line is approximately 20 m (70 ft.). It is unclear exactly what this depth shows. Although there are
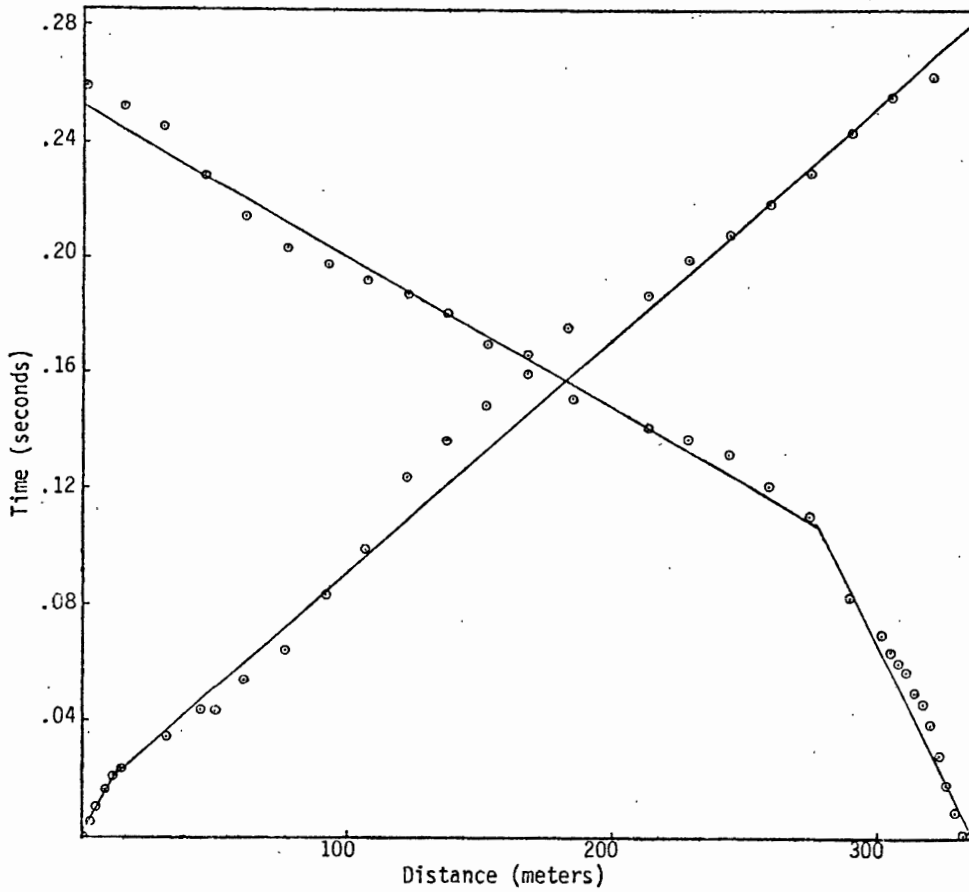
Figure 30. Refraction profile for line 2, southwest of fault.
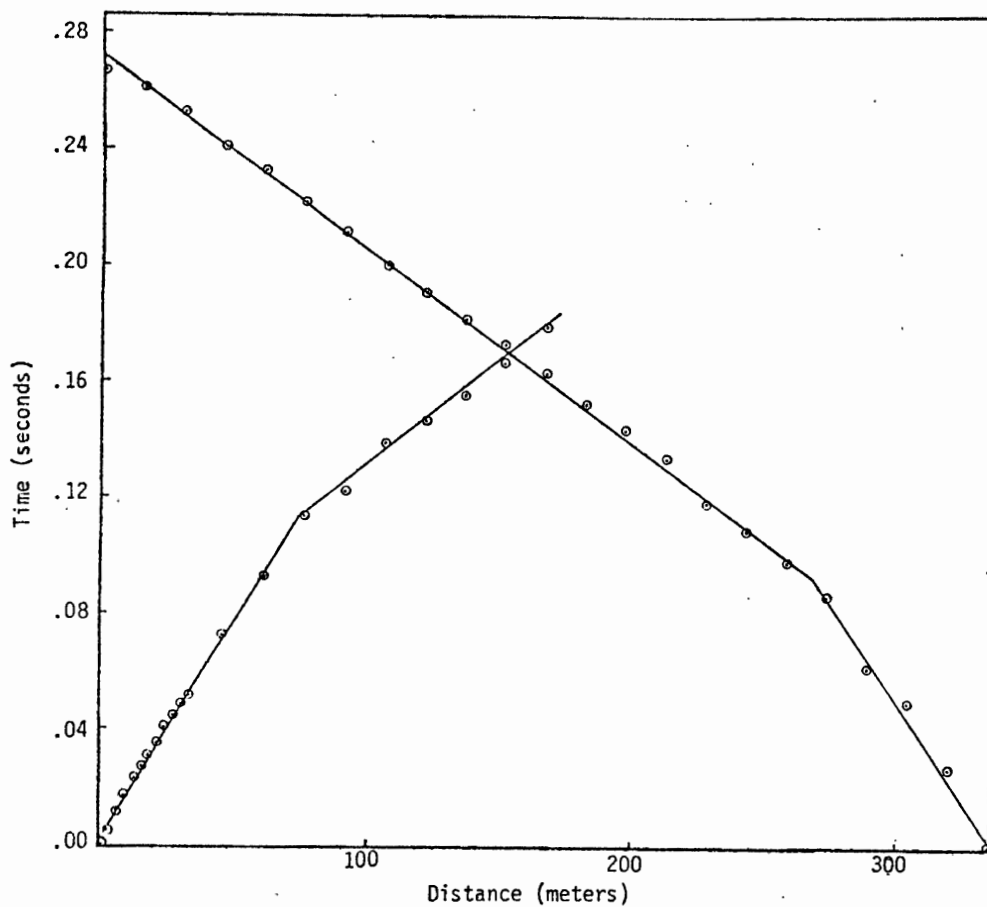
Figure 31. Refraction profile for line 3, across fault.
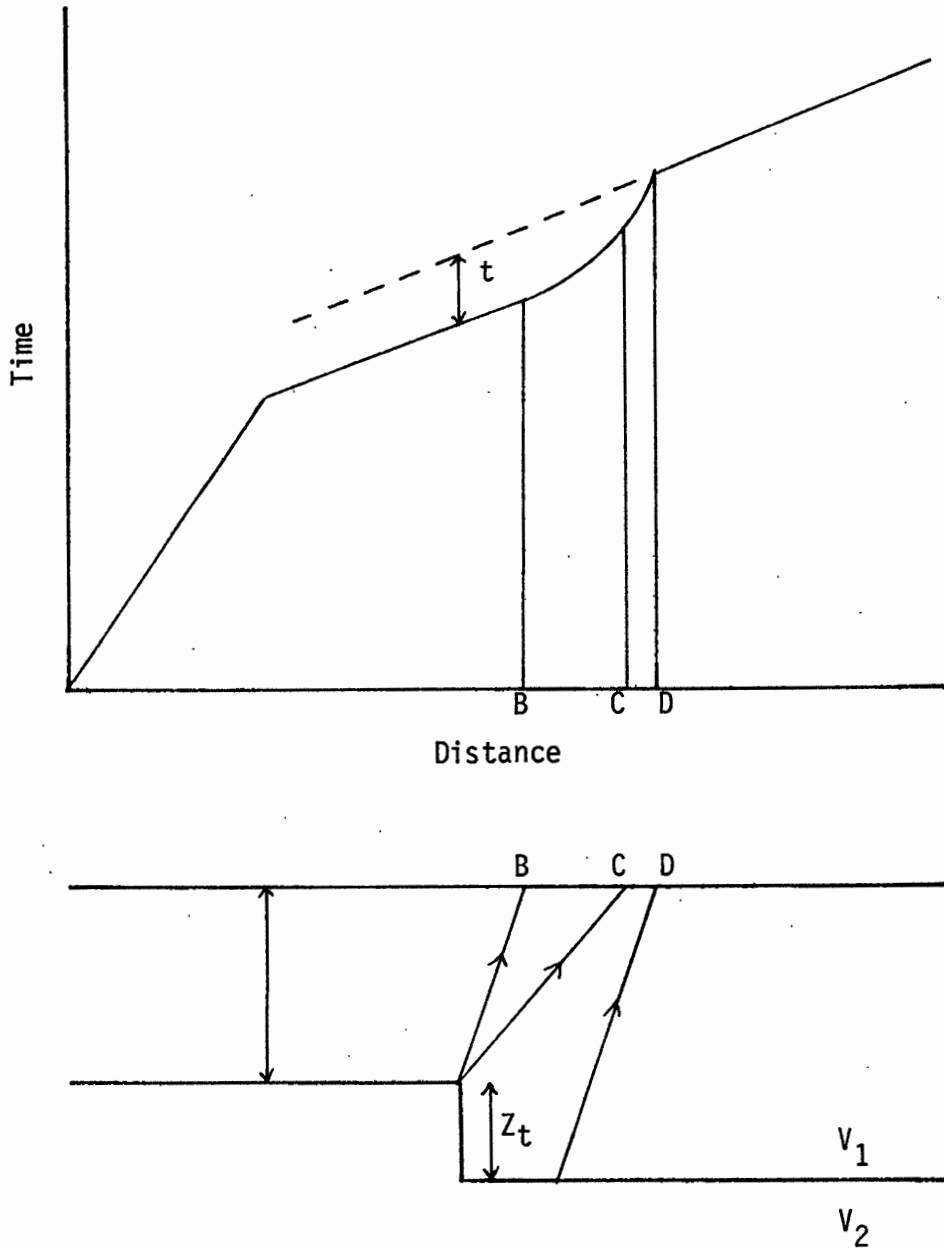
Figure 32. Refraction profile across a fault. Velocities of beds are V_1 and V_2; t is a measure of the throw of the fault (Dobrin, 1976).

no arrival times for the second half of the forward drop, this fact in itself shows that for some reason, the wave energy is not reaching the geophones after a certain point. The wave energy must travel somewhere; it may possibly be diffracted by fault gouge.

The refraction survey provided a check for the gravity models. Line 1, northeast of the fault, showed three layers: a surface layer with a depth of 12 m, a nearly horizontal tuff layer (see Figure 29), and a basalt layer. Line 2, southwest of the fault, showed a surface layer dipping to the north at approximately 5 degrees, underlain by tuff. Line 3, crossing the fault, showed two layers. Returns for the second half of the forward drop were not obtained, indicating that, for some reason, wave energy is lost in that area.

MAGNETICS

The intensity of the earth's magnetic field, like the gravitational field, depends on the type of rock the field is measured over. The magnetic field has both intensity and direction, whereas the gravitational field has magnitude only, the direction being essentially towards the center of the earth.

All magnets have two poles: a positive pole, which, when allowed to rotate freely, points in a general north direction, and a negative, or south-seeking pole. The force between two poles is given by the equation $F = 1/\mu(P_0 P/r^2)$, where P_0 and P are the strength of the two poles, r is the distance between them, and μ is the permeability of the material surrounding the poles, a dimensionless quantity. F is measured in dynes. The magnetic field strength at a point due to a pole of strength P at r distance away, is $P/\mu r^2$. When a magnetic material is placed in an external magnetic field, the material is polarized - magnetic poles are induced in the material. The intensity of magnetization, I, or the pole strength per unit area, is equal to $kH\cos\theta$ where H is the external field, θ is the angle of the field with the normal to the surface of the material, and k is the susceptibility of the material and is a measurement of its capability to be magnetized.

The susceptibility of a material is closely related to its magnetite content, and its variation in different rock types makes magnetic prospecting a useful tool. When a magnetic survey is conducted, the measurements are dependant on the susceptibility polarization, kH, and

the remnant polarization. For igneous rocks, remnant polarization is the directional polarization induced in the rock as it cooled from molten material in the direction of the earth's field at that time. For sedimentary rocks, the remnant polarization comes from the orientation of the grains with the earth's field as they were deposited. For most surveys, the susceptibility of the rocks is the distinguishing characteristic. Lateral changes in the earth's magnetic field result from lateral variations in rocks type. The closer the lateral variation is to the surface the sharper the anomaly (varying with $1/r^3$).

The magnetic field strength is measured in oersteds, which is one dyne per unit pole. The total magnetic field of the earth is approximately .5 Oe, so a smaller, more practical unit, the gamma, or 10^{-5} Oe is more commonly used.

Field Work.

The magnetic survey was conducted at the same time as the gravity survey, during February and March of 1979. After gravity readings for each line were taken, magnetic readings were taken at the same stations (Figure 7), with a Geometrics Proton Magnetometer. The unit consists of a sensor, staff, and console. After pressing a button, the total intensity of the earth's magnetic field in gammas is displayed. Three readings were taken at each station, and the average value used in constructing magnetic profiles. A base station was occupied approximately every hour, and those readings used to construct a drift curve for the measurements.

Interpretation.

Readings were corrected for drift, using base station readings. The data for each line was smoothed using Sheppard's five-term equation (Davis, 1973). In models that were tried, a susceptibility of .006 was used for basalt (Telford and others, 1976), and a susceptibility of 0 was used for the tuffs and other sediments, as most sediment susceptibility is negligible (Telford and others, 1976).

The magnetic contour map is shown in Figure 7. The data exhibits a strong linear trend, at an angle of 15 to 25 degrees to the fault. This is not unreasonable, as magnetic anomalies are aften displaced from the feature they delineate, (Hanson, 1966: pp. 49-50). However, if the trend is displaced it would be expected that the low would appear on the downdropped side of the fault. This is not the case. The magnetic profile for magnetic line B is shown over the model from the gravity analysis of that line in Figure 33. The low occurs northeast of the fault, over an area where sediments are quite shallow. If the data were rather irregular, it might be contributed to interference from power lines or underground pipes, but the trend exhibited by the data is very linear, and is consistent over several lines. Several simple models were tried to see if they could produce the same type of anomalies shown by the data.

One of the models, that of a thick horizontal slab representing a fault block (Dobrin, 1976), is shown in Figure 34. The slab represents basalt on the northeast side of the fault, with a susceptibility of .006. The thickness of the slab was 500 m, buried 25 m beneath the surface. The model does not fit the pattern of the magnetic profiles,

65
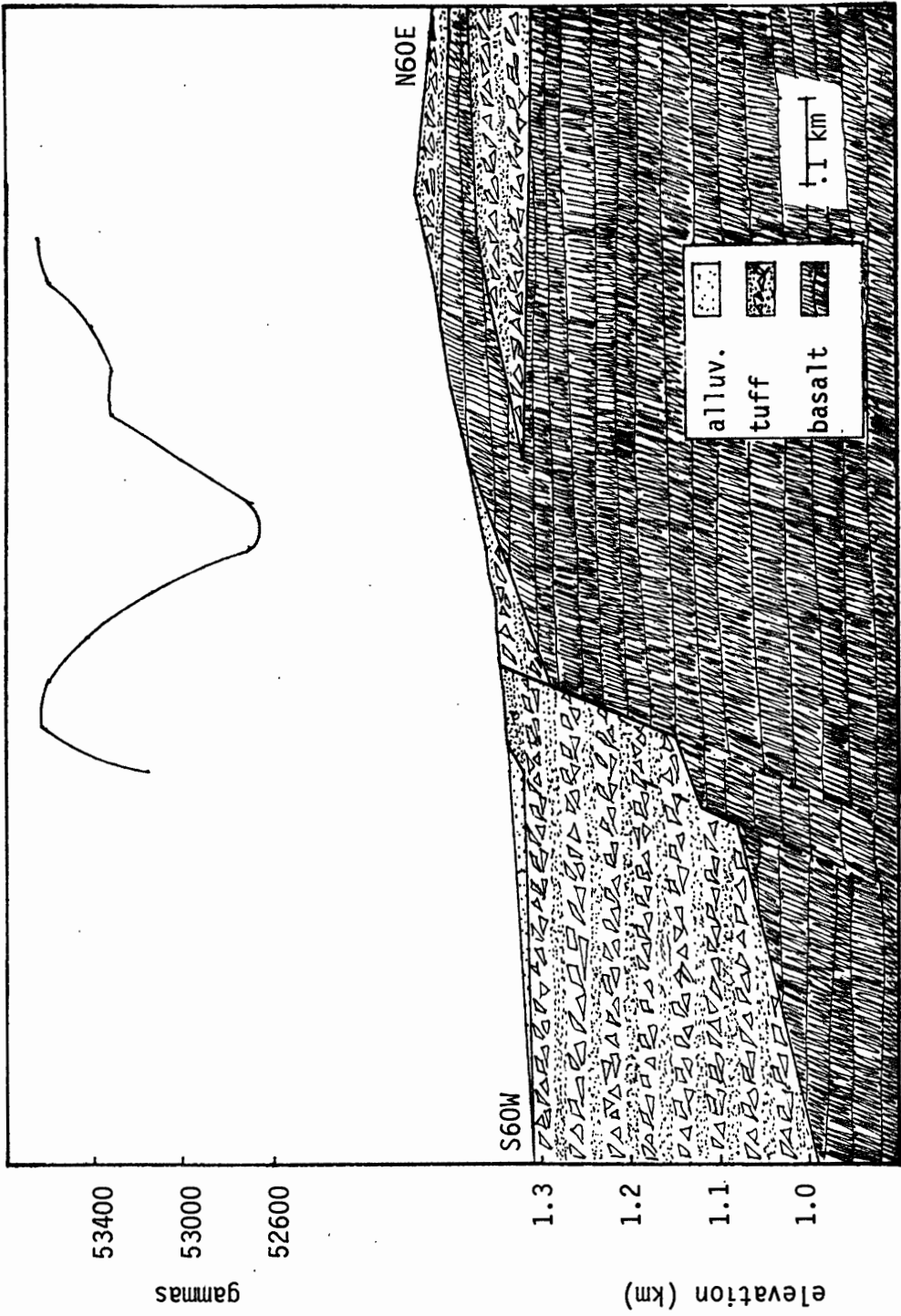
Figure 33. Plot of magnetic profile (line B) over gravity model of same line.
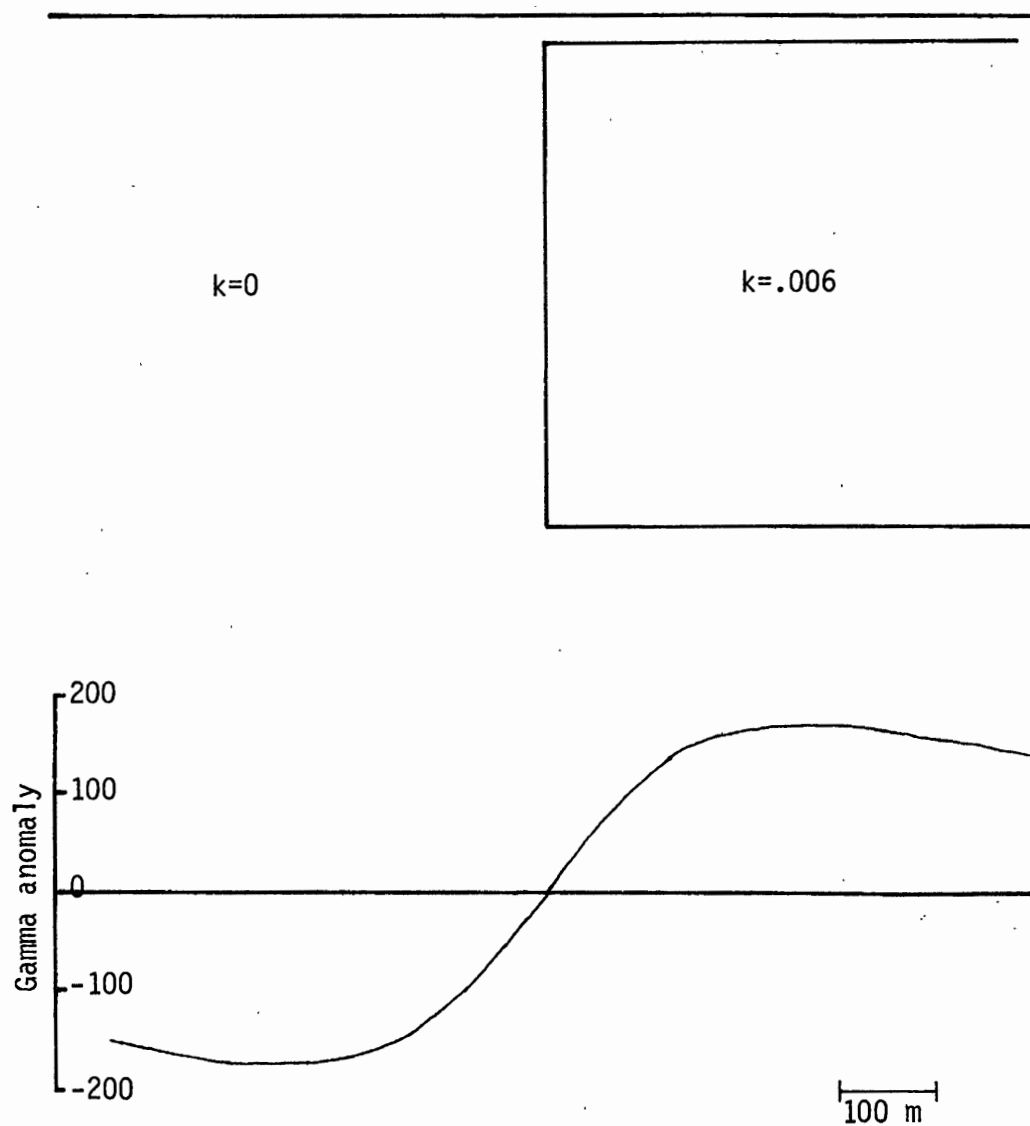
Figure 34. Magnetic profile and associated model for faulted
horizontal slab with susceptibility k=.006.

but shows a pattern similar to the one expected, a positive anomaly over the basalt and a negative anomaly over the tuff.

It is possible that the magnetic low over the basalt just northeast of the fault may be attributed to oxidation of magnetite in the fractures of basalt (M. Cummings, personal communication). Greatest oxidation may occur closest to the fault, where the basalt may come in contact with water traveling up the fault. This oxidation may reduce the magnetic susceptibility of the basalt near the fault and cause the magnetic low seen in the data.

The linear trend can most likely be associated with the fault. The low exhibited in the data could be imitated by any simple model, but may be due, as explained above, to oxidation of magnetite in basalt near the fault.

CONCLUSIONS

Gravity modelling and results from resistivity data, were used to accurately locate the fault exposed at one location on the campus of Oregon Institute of Technology. Refraction data provided a model check. Magnetic data appeared to be contradictory to the results of other methods, but may possibly be explained by oxidation of magnetite near the fault. The models are limited by the geologic control available and geologic reasoning, but outside of these limits, the models are somewhat arbitrary. Hopefully, after some experimentation, the preferred model is the most accurate representation.

A cross section based on data from four of the water wells on the campus of OIT defined two faults in the area; the second fault located between 45 and 75 m west of the exposed fault. The second fault was always included in the gravity modelling, and appeared to fit the gravity profile. Gravity modelling delineated the primary fault trending approximately N35W and dipping 65 degrees to the southwest. The tuff-filled, downdropped basin slopes to the north at approximately 10 degrees. Basalt flows interfinger with upper sediments on the downdropped side of the fault in the southernmost portion of the area, and thin to the north. This northward thinning is also evident in the geologic cross section. These basalt flows appear to thicken south of the study area, and may be the source of the gravity high located over Klamath Falls (Sammel and Peterson, 1976). Several layers of tuff are present on the upthrown side of the fault. The gravity modelling required the

presence of some low density material in this area, outcrops and well data provided some geologic control. The estimated thicknesses and depths of these tuff layers are somewhat arbitrary, however, resistivity profiles northeast of the fault indicated depths to the upper tuff layer in gravity line C.

Models of alternative dips and trends of the fault on gravity line A indicate a dip of approximately 65 degrees to be most appropriate, and the trend of the fault to be N35W (within four degrees).

Refraction data indicated a low density layer dipping north near the southwest ends of gravity lines A and B, consistent with a 2.0 g/cc density layer used in the gravity modelling of these lines. The refraction profile run northeast of the fault indicated that the tuff layer just north of the fault in gravity line B must meet the two tuff layers north of the fault in gravity line C. Refraction profiles run across the fault near gravity line C (Figure 7) did not give complete returns. A refraction line run across the fault near the north end of the area might better delineate a fault structure because of reduced subsurface interference with pipes and wells.

Magnetic data, rather than delineating sediment filled areas and basaltic areas with lows and highs, respectively, suggests almost the opposite. The explanation offered here is that the magnetic low observed in the data may be due to oxidation of magnetite in basalt near the fault. It is also possible that the data may be influenced by material outside of the study area. If this is true, a magnetic survey on a broader scale would be needed to delineate such a feature.

SOURCES CONSULTED

Berg, J. W., and Baker, C. D., 1963, Oregon earthquakes through
    1958: Seismol. Soc. Am. Bull., v. 53, pp. 95-108.

Berg, J. W., and Thiruvathukal, J. V., 1965, Gravity base station net-
    work, Oregon: Jour. Geophys. Res., v. 70, no. 4, pp. 3325-3330.

Bodvarsson, G., 1978, Zero frequency seismology: Oregon State University,
    Corvallis, Oregon, unpublished, 5 pp.

Breiners, S., Applications manual for portable magnetometer: GeoMet-
    rics Portable Proton Magnetometers, 58 pp.

Clark, S. P., 1966, Handbook of physical constants: Geol. Soc. Am.
    Memoir 97, 587 pp.

Davis, J. C., 1973, Statistics and data analysis in geology: New York,
    John Wiley and Sons, Inc., 550 pp.

Dobrin, M. B., 1960, Introduction to geophysical prospecting: New
    York, McGraw Hill Book Co., 446 pp.

Dobrin, M. B., 1976, Introduction to geophysical prospecting: New
    York, McGraw Hill Book Co., 630 pp.

Donath, F. A., and Kuo, J. T., 1962, Seismic refraction study of block-
    faulting, south-central Oregon: Geol. Soc. Am. Bull., v. 73,
    no. 4, pp. 429-434.

Hansen, D. A., 1966, Mining geophysics, Volume 1: Tulsa, Oklahoma,
    The Society of Exploration Geophysicists, 492 pp.

Jones, T. D., 1977, Analysis of a gravity traverse south of Portland,
    Oregon: Portland State University bachelor's thesis, 54 pp.

Nettleton, L. L., 1976, Gravity and magnetics in oil prospecting:
    New York, McGraw Hill Book Co., 464 pp.

Newcomb, R. C., 1958, Yonna Formation of the Klamath River Basin,
    Oregon: Northwest Science, v. 32, no. 2, pp. 41-48.

Peterson, N. V., and Groh, E. A., 1967, Geothermal potential of the
    Klamath Falls area, Oregon - a preliminary study: The Ore Bin,
    v. 29, no. 11, pp. 209-232.

Peterson, N. V., and McIntyre, J. R., 1970, The reconnaissance geology
    and mineral resources of eastern Klamath County and western
    Lake County, Oregon: Oregon Dept. Geol. and Min. Indus.,
    Bull. 66, 70 pp.

Sammel, E. A., and Peterson, D. L., 1976, Hydrologic reconnaissance
    at the geothermal area near Klamath Falls, Oregon: U. S. Dept.
    Interior Geological Survey, Open-File Report WRI 76-127, 127 pp.

Sharma, P. V., 1976, Geophysical methods in geology: New York, El-
    sevier, 428 pp.

Telford, W. M., Geldhart, L. P., Sheriff, R. E., and Keys, D. A., 1976,
    Applies geophysics: Cambridge, Cambridge University Press,
    860 pp.

Thiruvathukal, J. V., Berg, J. W., JR., and Henricks, D. F., 1970, Re-
    gional gravity of Oregon: Geol. Soc. Am. Bull., v. 81, no. 3,
    pp. 725-738.

VanDeusen, J. E., 1978, Mapping geothermal anomalies in the Klamath
    Falls, Oregon, region using gravity and aeromagnetic data:
    University of Oregon master's thesis, 87 pp.

Walpole, R. E., and Myers, R. H., 1978, Probability and statistics for
    engineers and scientists: New York, MacMillan Publishing Co.,
    Inc., 580 pp.

Weissenbom, A. E., ed., 1969, Mineral and water resources of Oregon:
    Oregon Dept. Geol. and Min. Indus. Bull 64, 462 pp.

APPENDIX A

Principal Facts for Klamath Falls Graben Fault Gravity Data

STATION	LATITUDE	LONGITUDE	ELEVATION	OBSERVED GRAVITY*	TERRAIN CORRECTION*	THEORETICAL GRAVITY*	FREE AIR ANOMALY*	SIMPLE BOUGUER ANOMALY*	COMPLETE BOUGUER ANOMALY*
64	42.2570°	121.7890°	1307.90 m	979984.96	0.76	980382.133	6.439	-139.751	-138.991
63	42.2573°	121.7884°	1312.13 m	979984.01	0.79	980382.160	6.769	-139.894	-139.104
62	42.2576°	121.7877°	1315.15 m	979983.51	0.80	980382.187	7.174	-139.827	-139.027
61	42.2578°	121.7870°	1316.40 m	979983.57	0.81	980382.204	7.601	-139.539	-138.729
60	42.2581°	121.7864°	1316.68 m	979983.97	0.88	980382.231	8.059	-139.112	-138.232
59	42.2584°	121.7858°	1316.31 m	979984.36	0.99	980382.258	8.309	-138.821	-137.831
58	42.2587°	121.7851°	1325.15 m	979982.91	1.15	980382.285	9.560	-138.558	-137.408
57	42.2590°	121.7844°	1332.95 m	979981.88	1.55	980382.312	10.911	-138.080	-136.530
56	42.2591°	121.7841°	1336.12 m	979981.41	1.20	980382.321	11.410	-137.935	-136.735
55	42.2593°	121.7836°	1336.15 m	979982.12	1.26	980382.339	12.112	-137.237	-135.977
42	42.2594°	121.7833°	1339.20 m	979981.75	1.32	980382.348	12.673	-137.016	-135.696
41	42.2596°	121.7830°	1339.99 m	979982.00	1.76	980382.366	13.150	-136.628	-134.868
40	42.2597°	121.7827°	1341.36 m	979981.72	1.41	980382.375	13.284	-136.647	-135.257
43	42.2598°	121.7824°	1343.31 m	979981.56	1.33	980382.384	13.717	-136.432	-135.102
44	42.2600°	121.7821°	1347.67 m	979980.95	1.50	980382.402	14.434	-136.202	-134.702
45	42.2601°	121.7818°	1351.30 m	979980.34	1.54	980382.411	14.935	-136.107	-134.567
46	42.2602°	121.7816°	1354.23 m	979979.83	1.58	980382.420	15.319	-136.050	-134.470
47	42.2603°	121.7813°	1353.34 m	979980.24	1.66	980382.429	15.447	-135.823	-134.163
48	42.2605°	121.7808°	1363.77 m	979978.24	1.80	980382.447	16.646	-135.789	-133.989
49	42.2607°	121.7803°	1369.77 m	979976.92	1.80	980382.465	17.161	-135.945	-134.145
50	42.2610°	121.7798°	1376.66 m	979975.54	1.90	980382.492	17.879	-135.997	-134.097
51	42.2612°	121.7791°	1387.60 m	979973.18	1.90	980382.510	18.878	-136.221	-134.321
52	42.2617°	121.7781°	1405.07 m	979969.76	1.42	980382.555	20.803	-136.248	-134.828
53	42.2620°	121.7774°	1409.06 m	979969.02	1.52	980382.582	21.268	-136.229	-134.709
54	42.2623°	121.7766°	1413.75 m	979967.89	1.36	980382.609	21.560	-136.462	-135.102
27	42.2563°	121.7823°	1335.27 m	979982.12	1.03	980382.070	12.108	-137.141	-136.111
26	42.2565°	121.7819°	1338.65 m	979981.36	1.06	910382.088	12.374	-137.253	-136.193
25	42.2566°	121.7816°	1341.61 m	979981.41	1.07	980382.097	13.328	-136.630	-135.560
24	42.2567°	121.7813°	1345.17 m	979980.91	1.09	980382.106	13.919	-136.437	-135.347
21	42.2569°	121.7809°	1348.44 m	979980.32	1.12	980382.124	14.318	-136.403	-135.283
20	42.2570°	121.7806°	1351.82 m	979980.11	1.15	980382.133	15.143	-135.957	-134.807

STATION	LATITUDE	LONGITUDE	ELEVATION	OBSERVED GRAVITY *	TERRAIN CORRECTION *	THEORETICAL GRAVITY *	FREE AIR ANOMALY *	SIMPLE BOUGUER ANOMALY *	COMPLETE BOUGUER ANOMALY *
22	42.2572°	121.7802°	1354.96 m	979979.54	1.22	980382.151	15.524	-135.927	-134.707
25	42.2573°	121.7799°	1360.08 m	979978.80	1.29	980382.160	16.355	-135.668	-134.378
28	42.2575°	121.7796°	1364.53 m	979977.82	1.35	980382.178	16.730	-135.790	-134.440
29	42.2576°	121.7793°	1369.71 m	979977.20	1.46	980382.187	17.700	-135.399	-133.939
30	42.2577°	121.7789°	1374.92 m	979976.44	1.49	980382.196	18.540	-135.142	-133.652
31	42.2580°	121.7783°	1388.70 m	979973.78	1.60	980382.222	20.104	-135.117	-133.517
32	42.2583°	121.7777°	1403.33 m	979970.62	1.54	980382.249	21.432	-135.425	-133.885
33	42.2585°	121.7771°	1410.92 m	979969.30	1.53	980382.267	22.436	-135.269	-133.739
34	42.2588°	121.7764°	1420.52 m	979966.80	1.46	980382.294	22.872	-135.906	-134.446
35	42.2592°	121.7754°	1439.24 m	979962.62	1.69	980382.330	24.432	-136.439	-134.749
106	42.2553°	121.7810°	1340.97 m	979981.98	0.99	980381.980	13.247	-136.640	-135.650
105	42.2555°	121.7807°	1342.46 m	979981.34	0.99	980381.998	13.620	-136.434	-135.444
104	42.2556°	121.7804°	1346.88 m	979980.56	1.13	980382.007	14.195	-136.353	-135.223
103	42.2558°	121.7800°	1348.37 m	979980.41	1.10	980382.025	14.488	-136.227	-135.127
100	42.2559°	121.7797°	1351.00 m	979980.20	1.14	980382.034	15.078	-135.930	-134.790
101	42.2561°	121.7794°	1354.78 m	979979.67	1.19	980382.052	15.696	-135.734	-134.544
102	42.2562°	121.7791°	1359.19 m	979978.97	1.25	980382.061	16.351	-135.573	-134.323
107	42.2563°	121.7788°	1364.50 m	979978.24	1.31	980382.070	17.249	-135.268	-133.958
108	42.2564°	121.7785°	1370.38 m	979977.15	1.40	980382.079	17.965	-135.209	-133.809
10	42.2532°	121.7816°	1344.02 m	979980.41	0.78	980381.791	13.376	-136.851	-136.071
9	42.2535°	121.7810°	1344.44 m	979980.77	0.84	980381.818	13.841	-136.434	-135.594
8	42.2538°	121.7803°	1342.46 m	979981.82	0.94	980381.845	14.253	-135.801	-134.861
7	42.2540°	121.7799°	1343.80 m	979981.54	0.95	980381.863	14.369	-135.835	-134.885
4	42.2541°	121.7796°	1346.18 m	979980.85	0.99	980381.872	14.403	-136.066	-135.076
3	42.2543°	121.7793°	1348.80 m	979981.77	1.04	980381.890	16.114	-134.648	-133.608
2	42.2544°	121.7789°	1352.70 m	979979.54	1.12	980381.899	15.079	-136.119	-134.999
1	42.2545°	121.7786°	1357.03 m	979978.56	1.16	980381.908	15.426	-136.256	-135.096
5	42.2547°	121.7783°	1361.45 m	979977.77	1.06	980381.926	15.982	-136.194	-135.134
6	42.2548°	121.7779°	1366.97 m	979976.73	1.48	980381.935	16.635	-136.157	-134.677
11	42.2550°	121.7775°	1378.37 m	979974.22	1.67	980381.953	17.625	-136.442	-134.772
12	42.2551°	121.7772°	1387.51 m	979972.75	1.42	980381.962	18.968	-136.121	-134.701
13	42.2553°	121.7769°	1392.81 m	979971.74	1.64	980381.980	19.577	-136.105	-134.465
14	42.2555°	121.7762°	1410.77 m	979967.92	1.56	980381.998	21.279	-136.410	-134.850
15	42.2557°	121.7758°	1423.60 m	979964.95	1.69	980382.016	22.251	-136.872	-135.182
16	42.2562°	121.7748°	1419.27 m	979964.56	1.45	980382.061	20.480	-138.159	-136.709
205	42.2534°	121.7795°	1344.84 m	979981.45	0.80	980381.809	14.652	-135.667	-134.867
204	42.2535°	121.7792°	1346.82 m	979981.07	0.94	980381.818	14.875	-135.666	-134.726
203	42.2537°	121.7788°	1350.05 m	979980.26	1.10	980381.836	15.044	-135.858	-134.758
200	42.2538°	121.7785°	1355.54 m	979979.24	1.27	980381.845	15.708	-135.807	-134.537
201	42.2539°	121.7782°	1362.21 m	979977.75	1.40	980381.854	16.269	-135.992	-134.592
202	42.2541°	121.7779°	1368.03 m	979976.65	1.36	980381.872	16.947	-135.965	-134.605
207	42.2542°	121.7775°	1376.39 m	979974.94	1.70	980381.881	17.881	-136.040	-134.340

STATION	LATITUDE	LONGITUDE	ELEVATION	OBSERVED GRAVITY*	TERRAIN CORRECTION*	THEORETICAL GRAVITY*	FREE AIR ANOMALY*	SIMPLE BOUGUER ANOMALY*	COMPLETE BOUGUER ANOMALY*
208	42.2543°	121.7772°	1384.31 m	979973.16	1.82	980381.890	18.462	-136.269	-134.449
90	42.2500°	121.7831°	1320.58 m	979986.23	0.68	980381.504	12.250	-135.357	-134.677
89	42.2503°	121.7824°	1321.22 m	979986.32	0.81	980381.531	12.511	-135.168	-134.358
83	42.2507°	121.7816°	1324.05 m	979986.09	1.01	980381.567	13.120	-134.876	-133.866
87	42.2511°	121.7807°	1338.44 m	979983.05	0.88	980381.603	14.484	-135.120	-134.240
86	42.2513°	121.7801°	1342.25 m	979982.51	0.87	980381.621	15.101	-134.928	-134.058
85	42.2516°	121.7794°	1345.66 m	979982.23	0.92	980381.648	15.848	-134.563	-133.643
84	42.2519°	121.7787°	1353.25 m	979980.89	1.09	980381.675	16.823	-134.437	-133.347
73	42.2521°	121.7783°	1358.07 m	979980.01	0.97	980381.693	17.411	-134.387	-133.417
72	42.2522°	121.7780°	1362.09 m	979978.97	1.10	980381.702	17.604	-134.644	-133.544
71	42.2524°	121.7777°	1367.30 m	979977.90	1.25	980381.719	18.124	-134.706	-133.456
70	42.2525°	121.7774°	1373.55 m	979976.63	1.22	980381.728	18.774	-134.755	-133.535
74	42.2526°	121.7772°	1380.80 m	979974.78	1.30	980381.737	19.153	-135.186	-133.886
75	42.2527°	121.7769°	1390.99 m	979972.79	1.64	980381.746	20.296	-135.182	-133.542
76	42.2528°	121.7767°	1400.13 m	979971.02	1.87	980381.755	21.339	-135.161	-133.291
77	42.2529°	121.7764°	1413.36 m	979968.04	1.99	980381.764	22.432	-135.546	-133.556
78	42.2530°	121.7761°	1423.42 m	979965.84	2.07	980381.773	23.327	-135.775	-133.705
79	42.2533°	121.7755°	1433.23 m	979962.27	2.08	980381.800	22.759	-137.441	-135.361
80	42.2536°	121.7749°	1434.45 m	979962.20	1.51	980381.827	23.038	-137.298	-135.788
81	42.2538°	121.7743°	1436.83 m	979962.20	1.16	980381.845	23.754	-136.848	-135.688
82	42.2541°	121.7736°	1443.69 m	979961.18	1.11	980381.872	24.823	-136.545	-135.435
83	42.2548°	121.7720°	1443.72 m	979962.05	1.06	980381.935	25.640	-135.732	-134.672
1000	42.2550°	121.7850°	1319.78 m	979984.48	0.64	980381.953	9.807	-137.712	-137.072
2000	42.2576°	121.7757°	1422.44 m	979966.18	1.50	980382.187	22.953	-136.041	-134.541

* numbers in mgals